INTEGRATING DISCRETE-RETURN SCANNING LIDAR AND SPACEBORNE RADAR TO SUPPORT ABOVEGROUND BIOMASS ASSESSMENTS

by

Olivier W.L. Tsui

B.Sc., McGill University, 2000

A THESIS SUBMITTED IN PARTIAL FULFILLMENT OF

THE REQUIREMENT FOR THE DEGREE OF

MASTER OF SCIENCE

in

The Faculty of Graduate Studies

(Forestry)

The University of British Columbia

(Vancouver)

March 2013

Abstract

Forests are considered important reservoirs of organic carbon and have been identified as essential in moderating climate change. Measuring the amount of carbon stored in forests helps improve our understanding of the carbon budget and help with climate change adaptation strategies. Therefore, effective and accurate methods in characterizing changing forest cover and biomass densities are needed.

Both LiDAR (light detection and ranging) and radar (radio detection and ranging) technologies can contribute towards the study of forest biomass but one sensor alone cannot provide all the information necessary to monitor forests. Understanding and investigating synergies between different remotely sensed data sets provides new and innovative opportunities to monitor forests.

The overall objective reported in this thesis is to demonstrate novel methods to integrate two remotely sensed data sets (i.e., radar and LiDAR) for the application of biomass estimation. This research was divided into two main questions: (1) can shorter wavelength radar variables provide improved biomass estimates when combined with LiDAR data; and (2) can the use of space-borne radar extend aboveground biomass estimates over a larger area using spatial modeling methods.

In the first study, relationships between biomass and biomass components with LiDAR and radar data were examined through regression analyses to determine the best combined parameters to estimate biomass. Results indicated that integrating radar variables to a LiDAR-derived model of aboveground biomass helped explain an additional 17.9% of the variability in crown biomass. This corresponded in an improvement in crown biomass estimates of 10%

RMSE. Furthermore, InSAR coherence magnitudes from C-band and L-band radars provided the best estimate of aboveground biomass using radar alone.

In the second study, aboveground biomass transects derived from plot-based field data and LiDAR, and wall-to-wall radar were spatially integrated using three kriging techniques. The results indicated the importance of correlation between primary and secondary variables when using these kriging approaches. Also a 1000 m distance between biomass transects, was found to provide reasonable compromise between ease of use, accuracy, and cost of obtaining LiDAR data for the study area. Insights into other opportunities for further development in spatial modeling techniques are discussed.

Preface

This thesis is the combination of two scientific papers of which I am the lead author. The structure and design of the project developed over time with guidance from Dr. Nicholas C. Coops, Dr. Michael A. Wulder, and Dr. Peter L. Marshall with the purpose of investigating methods to integrate different active remote sensing technologies for aboveground biomass assessments.

For both scientific journal submissions, I performed the primary research including data collection, data analysis, and interpretation of results and prepared the final manuscripts. A portion of the data analyzed was compiled from pre-existing sources collected by Dr. Nicholas C. Coops and Dr. Thomas Hilker. Overall project oversight, advice on methodology and editorial comments were provided by Dr. Nicholas C. Coops. Dr. Michael A. Wulder provided guidance in forestry principles and on LiDAR technology and background as well as invaluable editorial comments. Dr. Peter L. Marshall provided suggestions and comments on statistical analyses and also invaluable editorial comments. Mr. Adrian McCardle completed all InSAR processing for the first scientific publication. Mr. Grant Bruce provided suggestions and editorial comments.

Publications arising from this thesis include (reprinted with the permission from the publishers):

- Chapter 3: **Tsui, O.W.**, Coops, N.C., Wulder, M.A., Marshall, P.L., and McCardle, A., 2012. Using multi-frequency radar and discrete-return LiDAR measurements to estimate aboveground biomass and biomass components in a coastal temperate forest. ISPRS Journal of Photogrammetry and Remote Sensing 69, 121–133.

- Chapter 4: **Tsui, O.W.,** Coops, N.C., Wulder, M.A., and Marshall, P.L., 2013. Integrating airborne LiDAR and space-borne radar via multivariate kriging to estimate aboveground biomass. *Remote Sensing of Environment. (submitted)*

Table of Contents

List of Tables

List of Figures

Glossary

Alpha:
A decomposition variable that provides the dominant scattering mechanism of the microwave pulse.

Backscatter:
The amount of energy returned to the radar sensor following an interaction (e.g. scattering) with a ground target.

Coherence:
Parameter that describes the relative difference in oscillation between two microwave pulses. In other words, measures the degree of correlation between two microwaves.

Entropy:
A decomposition variable that provides a measure of the randomness in the scattering recorded by the radar sensor.

InSAR:
Interferometric synthetic aperture radar (InSAR) is a radar processing technique to generate maps of surface deformation and elevations using two or more radar images.

LiDAR:
Light Detecting and Ranging, an active optical remote sensing technology that measures the distance to targets through emitted near infra-red light pulses.

Polarimetry:
The measurement and interpretation of polarization of transverse waves (e.g. microwaves).

Polarization (HH, HV, VV):
Orientation and alignment of the microwave pulse in a plane perpendicular to the direction of propagation. Radars can emit microwaves that are horizontally oriented or vertically oriented and receive the same or different orientation.

Pol-InSAR:
Polarimetric interferometric SAR, is the processing of InSAR using radar data that is fully polarimetric (e.g. contains all information on the polarization of the microwave).

Radar bands:
Categories that classify the microwave portion of the electromagnetic spectrum based on their frequency or wavelength are called bands. Most common spaceborne remote sensing bands are X-, C-, and L-band.

RADAR:
Radio Detecting and Ranging, an active microwave remote sensing technology that maps the electromagnetic scattering coefficient onto a 2-dimensional plane. Synthetic aperture RADAR (SAR) is similar but mainly spaceborne and simulates an extremely large antenna to generate high resolution images.

Acknowledgements

This research was undertaken with funding from the National Sciences and Engineering Research Council of Canada (NSERC) Engage Grant, a Discovery grant to Dr. Nicholas C. Coops, and Hatfield Consultants Partnership. All RADARSAT-2 data were provided through the Canadian Space Agency's RADARSAT-2 Science and Operational Applications Research Education Initiative (SOAR-E). I thank Dr. Andrew Black and the BIOMET members for allowing us access to the FLUXNET-Canada site. I also thank the forest companies Timberwest and Island Timberlands for providing their forest inventories and allowing access to their private lands. Furthermore I would like to thank Colin Ferster, Jean-Simon Michaud, and Martin van Leeuwen for their help collecting field data, and to 3V Geomatics for InSAR processing of all radar data.

Special thanks to my supervisor, Dr. Nicholas C. Coops, who provided his time and a great deal of patience during my degree. I thank each of the committee members, Dr. Michael A. Wulder, Dr. Peter L. Marshall, and Mr. Grant Bruce for their support and insight. I am also grateful to all partners at Hatfield Consultants for their encouragement and support throughout my degree. Lastly, I also would like to acknowledge all member of the IRSS lab, past and present, for openly offering their knowledge, support, and company.

To my family and friends for their words of encouragement, and to Wanda for her love and support.

1. INTRODUCTION

1.1 Terrestrial Carbon Cycle

The complex biogeochemical processes through which carbon is exchanged between the biosphere, geosphere, atmosphere, and hydrosphere is known as the global carbon cycle (Schlesinger and Andrews, 2000). The exchange between atmospheric gasses and the terrestrial biosphere occurs through carbon uptake by vegetation and through carbon release by plant respiration, soil respiration, and land disturbance processes (Prentice et al., 2001). Plants convert carbon dioxide to organic carbon by absorbing solar radiation through the process of photosynthesis. This carbon storage in the form of vegetation biomass, accounts for half of the living mass of terrestrial vegetation (Johnson and Sharpe, 1983); therefore, forests are considered a large reservoir of carbon (Dixon et al., 1994). Current global forest carbon stocks are estimated at 861 ± 66Pg C (Pan et al., 2011). As a whole, terrestrial carbon sinks may be responsible for the uptake of one third of all carbon dioxide emissions released by anthropogenic activities (i.e., fossil fuels and land use change) into the atmosphere (Canadell et al., 2007). In contrast to other carbon pools (i.e., soil carbon), forests can be more easily characterized and monitored through various methods, such as remote observations and field inventories. Consequently, loss and gain dynamics in forest carbon can be quantified and the impacts of various forest land management approaches on carbon storage assessed. Measuring the amount of carbon stored in forests can play an important role in improving our understanding of the carbon budget and help with strategies aimed at mitigating climate change (Song, 2012).

1.2 Climate Mitigation

Due to increasing CO_2 levels we are in a period of rapid climate change (Peters et al., 2013). The impacts of climate change on many natural systems, such as increase shifts in species'

geographical ranges, increase wildfire risks, decrease water availability, etc., are documented and reported by the Intergovernmental Panel on Climate Change (IPCC) (IPCC, 2007). Atmospheric concentration of greenhouse gasses (GHGs) such as CO_2 and modified land cover are key drivers of these changes (Pan et al., 2011; Peters et al., 2013). Numerous studies have investigated the potential impacts and vulnerabilities of climate change on physical and biological processes (Bellard et al., 2012; Coops and Waring, 2011; Parmesan and Yohe, 2003; Zhu et al., 2012). Impacts on forest vegetation from changing climate will increasingly affect forest ecosystems processes (Metsaranta et al., 2011), with gradual increases in temperature, changes in rainfall patterns or modification of atmospheric conditions such as cloud cover, will also likely impact vegetation growth, regeneration and natural rates of mortality (Chapin et al., 2010).

A reduction in the rate of carbon accumulation in the atmosphere is required to mitigate climate change. This can be achieved through a decrease in GHG emissions generated from burning of fossil fuels and by increasing the net uptake (or reducing the net loss) of carbon in terrestrial ecosystems (Kurz and Apps, 2006). Information on the vertical and horizontal characteristics of forests is therefore increasingly important. Due in part to global initiatives, such as the UNFCCC (United Nations Framework Convention on Climate Change) (UNFCC, 2007), and international reporting obligations, that are aimed at better understanding global GHG sources and sinks, detailed information on forested land and the impacts of human activities are being collected that will facilitate better understanding of changes in forest carbon stock.

In Canada, forest carbon stock and its change are assessed through initiatives such as the national forest carbon monitoring accounting and reporting system (Kurz et al., 2009). This carbon accounting system integrates, at different temporal and spatial scales, information on

land use change, statistics on disturbance events, growth and yield information, and detailed forest inventory data, into a modeling framework (i.e. Carbon Budget Model of the Canadian Forest Sector - CBM-CFS3) to estimate carbon stock and changes in carbon (Kurz et al., 2009).

However, in contrast to countries with established forest inventories and monitoring programs, such as Canada, many non-annex I countries (i.e., developing countries), have large forested areas that are not well characterized because of a lack of consistent and uniform systematic forest inventories (an important component for an operational measurement, reporting, and verification (MRV) system)(Grainger and Obersteiner, 2011).

Under the UNFCCC, discussions are in progress to develop a mitigation strategy to reduce emissions from deforestation and forest degradation (REDD), and promote the role of conservation, sustainable management of forests and enhancement of forest carbon stocks in developing countries (REDD+). While the initial aim for REDD was to slow, halt, or reverse forest cover and carbon loss by placing monetary value on the amount of carbon stored in forest land (Pistorius, 2012; Tacconi et al., 2010; van de Sand, 2012), REDD+ aims to also promote enhancement of carbon storage and conservation by including a wider range of stakeholders (Campbell, 2009; Romijn et al., 2012). REDD+ implementation is available to national or local governments, non-governmental organizations (NGOs – CARE, WWF), and the private sector who are interested in offsetting their carbon footprint. Through the retention of carbon, and thus the avoidance of emissions from deforestation, carbon credits produced can be traded on voluntary carbon markets (Corbera et al., 2009; Kimberly and Curran, 2009; Miles and Kapos, 2008).

These performance-related payment schemes for environmental services (PES) are only likely to work if the value of the environmental services exceeds opportunity costs of the land holders (Campbell, 2009). In other words, if it is financially justifiable to diverge from business as usual

scenarios. While recognizing the limitations, problems, and current discussions on the effectiveness associated with placing a value on forests and their carbon alone (Kimberly and Curran, 2009), a price for an area of forest can only be assessed if the carbon stock of an area can be accurately determined with known error. In order to determine forest carbon stocks per unit area, spatially explicit data on aboveground biomass are important. Guidelines released by the IPCC provide three tiers for carbon emission reporting, with Tier 1 having the highest uncertainty but being the easiest to implement and Tier 2 and Tier 3 having the lowest uncertainty but most difficult to implement. Recommendations are for higher tiers; however, higher tier methods require more data and are more expensive, because they involve monitoring of local variables, such as aboveground biomass and carbon stock changes (Romijn et al., 2012).

Although emission reduction activities in Canada are not eligible under the REDD+ framework, there are a number of voluntary carbon offset programs and protocols that have been developed for Annex I countries (Ristea and Maness, 2009). For example, the Emission Offsets Regulation (British Columbia, 2008) and the Forest Carbon Offset Protocol of British Columbia (British Columbia, 2011) were designed to help guide, design, quantify, and verify carbon offsets projects on private and public land. In Canada, forested land are primarily owned and managed by the crown; therefore, provincial governments have the mandate to sustainably manage forest resources and promote a broader range of non-timber services. Furthermore, sound management practices are driven not only by economic evaluation of forests but social perception, in other words the value of forests for non-timber values (Harshaw et al., 2009). As a result, a wide spectrum of stakeholders, from regional to local governments, private sector entrepreneurs, conservation agencies, and First Nations, are interested in forest carbon offset projects (Greig and Bull, 2011). With such a wide range of stakeholders, new technologies and innovative methods to estimate biomass accurately are important.

1.3 Forest Biomass Estimation

Components of forest biomass include aboveground (AGB) and belowground biomass (BGB). AGB consists of all living material above the soil, including stem, trunk, branches, bark, and foliage; and BGB consists of all live roots greater than 2mm in diameter (Penman et al., 2003). Although it is recognized that BGB is an important component in determining the entire forest carbon stock, for simplicity the term biomass will refer to AGB for the remainder of this thesis.

Accurate estimates of biomass play an important role in understanding the carbon cycle. Direct measurements of AGB require destructive sampling of trees (i.e., harvesting of trees, oven-drying all components, and then weighing them) (Brown, 1997). Given the inefficiency of this method, a more practical approach in estimating biomass is to use allometric equations, which are developed from destructive harvesting, and relating the mass of foliage, branches, bark and trunks to direct structural measurements, such as diameter at breast height (DBH) and tree height (Lambert et al., 2005). Information on forest and structural characteristics are often obtained by statistical sampling and the use of ground plots, which form the basis for forest inventories (Kangas et al., 2006). Air photos are also commonly used to aid forest inventories by identifying and mapping homogeneous units based on relevant forest attributes such as age, species composition, volume, and stand structure (Gillis and Leckie, 1993). However, obtaining comprehensive, spatially complete, and accurate forest inventory data is usually costly, labour intensive, and limited to smaller areas (Kangas et al., 2006). Remotely-sensed data acquired from satellite or aerial platforms has provided a practical and economical means to measure and monitor vegetation cover and structure, especially over large areas (Xie et al., 2008).

Optical remote sensing data are commonly used for land cover mapping, capture of change, empirical estimates of structural attributes, and to provide strata for statistical attribute estimation. The estimation of biomass with optical data is also well established; see Lutz et al.

(2008) for a review. However, direct biomass estimates at the landscape and/or the regional level still pose some challenges (Gibbs et al., 2007). Optical remote sensing data provides limited information on the vertical distribution of forest structure (Wulder, 1998). Typically, once crown closure is reached there is little spectral difference between stands with increasing structural complexity and, as a result, estimates of biomass, leaf area, and volume derived from optical imagery tend to reach an asymptote (i.e., signal saturation level), whereby further increases in biomass are not detectable (Duncanson et al., 2010). While experimental trials over smaller areas can show greater range (Song, 2012), mapping small differences at high biomass levels with optical sensors is difficult and have not proven to be consistent over large areas (Goetz et al., 2009). Furthermore, the presence of clouds, shadows, and haze can impact the quality and completeness of optical data, especially in tropical areas (Roy et al., 2010). However, new means of optical image processing are providing novel opportunities for composting that may mitigate the negative impacts of cloud cover (Hansen and Loveland, 2012).

A number of remote sensing technologies that have experienced a great deal of scientific and operational attention in the last few years for forest biomass estimation include radar based approaches including space-borne synthetic aperture radar (SAR) (Santoro et al., 2011; Thiel et al., 2009), and interferometric SAR (InSAR) (Simard et al., 2006), and LiDAR (light detection and ranging) (Næsset et al., 2011). Unlike optical sensors, which passively record reflected energy, active system supply their own energy and record the portion of the energy reflected back at the sensor. In the case of radars, sensors emit microwave pulses and records the strength of the returning pulse, also known as backscatter, after some surface interaction (Woodhouse, 2005). Backscatter is strongly dependent on radar frequency, polarization of the microwave, and the shape, size, and moisture content of the ground target. As a result, radar sensors are able to record direct interaction with groups of trees and can provide structural measurements

important in estimating forest biomass (Sader et al., 1989). Current SAR platforms operate at different frequencies or microwave wavelengths, the most common being: X-band (3.0 cm); C-band (5.6 cm); L-band (24 cm); and P-band (74 cm). Theoretical scattering models of forest have shown that at longer wavelengths (L or P-band), signal returns due to scattering result mainly from tree branches, trunks, and ground surfaces; while at shorter wavelengths, smaller branches and leaves drive the scattering (Kasischke et al., 1997). Provision of its own illumination source also allows SAR sensors to transmit microwave signals that are either horizontally (H) or vertically (V) polarized, relative to the Earth's surface and record the returned signal in either of these polarizations. This ability to operate in multiple polarization modes, from single polarization (transmit H or V; receive H or V), dual polarization (transmit H or V; receive H and V), or quad-polarization (transmit H and V on alternate pulses; receive H and V on every pulse) provides additional information about forest and canopy structural characteristics.

Scattering of the microwave pulse is strongly dependent on the frequency and polarization of the microwave pulse, and the shape, size, orientation, and moisture content of the target. Radar sensors are, therefore, able to record direct interaction with structural elements and can provide measurements important in estimating AGB (Sader et al., 1989). Quantifying biomass using SAR data have been demonstrated by many studies (Dobson et al., 1992; Le Toan et al., 1992; Lucas et al., 2006). Unfortunately, signal return for all SAR frequencies saturate and limit the predictive capability at moderate to high biomass levels, especially when higher frequencies are used (Imhoff, 1995a). In addition to saturation effects at high biomass levels, challenges with using SAR may include poor accuracy and temporally unstable relationships due to variability in weather conditions such as frost and wind (Kasischke et al., 2011; Ranson and Sun, 1997). However, with its capacity to collect usable data over a wider range of weather

conditions and provide frequent observations, SAR data can provide generalized information on the horizontal distribution of forests at stand and regional scales suitable across large areas.

The possible use of InSAR for assessing biomass is also of interest due to the demonstrated provision of height measurements with no apparent saturation limit. For example, Solberg et al. (2010) showed the effective use of single-pass X-band InSAR data for measuring forest biomass in the boreal region of southern Norway and reported a linear relationship between biomass and InSAR heights with no apparent saturation effect. However, obtaining accurate height measurements requires reducing or compensating for temporal decorrelation, which necessitates the use of multiple baselines to improve interferometric processing or the use of single-pass interferometry. These requirements lower operational uptake given that there are no space-borne L- or P-band SAR satellites currently operational, and no SAR sensors with single-pass configuration, with the exception of TanDEM-X lunched in 2010, primarily designed to provide detailed digital elevation model (DEM) data.

In contrast, airborne laser scanning or LiDAR sensors measure the distance between the sensor and the target (e.g., the ground or tree canopy) based on half the elapsed time between the emitted laser pulse and the recorded return pulse (Næsset, 1997). This allows LiDAR systems to accurately measure the vertical structural characteristics of trees and use this information to estimate forest stand characteristics, such as stand density, aboveground biomass, and basal area (Lefsky et al., 1999; Lim and Treitz, 2004; Næsset and Gobakken, 2005; Næsset, 2002). Published studies have demonstrated the non-asymptotic relationship between LiDAR structural measurements and biomass (Lefsky et al., 1999) and the accuracy of canopy or individual tree height measurements (Næsset and Økland, 2002).

Although accurate, the use of LiDAR data for large area monitoring is challenging because of operational considerations that limit widespread use, such as high data acquisition costs,

aircraft scheduling and logistics, and large data volumes (Wulder et al., 2008a). Although costs have generally decreased, a review by Wulder et al. (2008a) discusses several factors that can affect cost. For instance, improvements in pulse rates enable flying higher which means fewer lines are required to cover an area with the desired hit density; however, fuel costs, especially for remote locations, can be a key cost driver. Given the inverse relationship between spatial coverage and spatial resolution (Franklin et al., 2002), cost may be the primary obstacle in using LiDAR for large-area forest characterizations (Wulder and Seemann, 2003). Even with anticipated reductions in LiDAR data costs in the near future (Li et al., 2008), it is still unlikely that LiDAR data would be used to provide wall-to-wall forest characterization measurements for large or remote locations (Wulder et al., 2012b). However, there are an increasing number of examples where the expense in LiDAR collection is justified by information requirements, such as the motivation for elevation data (Woods et al., 2011). A summary of the advantages and disadvantages in the use of airborne LiDAR or space-borne radar to estimate forest biomass are provided in Table 1.1.

Table 1.1 Benefits and limitations of airborne LiDAR and spaceborne SAR in estimating forest biomass.

	Advantages	Disadvantages
LiDAR	• Direct biophysical measurement of vertical structure. • High accuracy and precision in estimating forest biomass.	• Small-footprint can be cost prohibitive for larger areas depending on application.
SAR	• Observations over large areas. • Acquire usable data under a range of weather conditions. • Able to provide biomass estimates for different components (e.g., trunk, branches, canopy, etc.).	• Asymptotic relationship at moderate to high biomass levels. • Poor accuracy and sensitive to topography and moisture content due to dielectric properties.

1.4 Data Integration

Unfortunately, there is no single remote sensing technology capable of providing all the information necessary to characterize forests completely, and obtaining detailed vertical measurements for large areas (De Sy et al., 2012). Therefore, studies conducted in the last two decades have focused on exploiting the strengths of each of these remote sensing technologies. Although studies have investigated the relationship of SAR and LiDAR measurements to forest biomass separately (Koch, 2010), recent studies have examined the benefits and synergies of integrating LiDAR and SAR data. Given the complimentary match of information that exists between radar and LiDAR data (Hyde et al., 2006; Wulder et al., 2012a), additional analysis options should be promoted and investigated. For example, forest biomass estimates derived from LiDAR data can be used to calibrate, and subsequently validate, wider area observations made by radar. In general, the use of multiple data sources can increase cost-efficiencies, resolve data coverage, and cloud cover issues; however, using multiple data sources also increases complexity of the analysis (De Sy et al., 2012). A few relevant studies on LiDAR and radar, and their integration, for biomass estimation are summarized in Table 1.2.

Effective and accurate methods in mapping and monitoring AGB are needed, especially for areas where limited or no inventory data are available or persistent cloud cover is an issue. The large spatial coverage and dynamic nature of forests can also complicate quantifying forest biomass; however, each of the remote sensing technologies presented, provides a particular advantage in measuring forest biomass. Integrating the complimentary information derived from LiDAR and radar has the potential to overcome some of these challenges inherent in any one approach.

Table 1.2 Sample studies in radar and LiDAR for forest characterization, including AGB estimation, and their key research findings.

Author	Vegetation Type	Method	Data Sources	Key Findings
SAR and InSAR				
Le Toan et al., 1992	Maritime Pine	Regression analysis	SAR (P, L,C-band at HH, HV, VV polarization)	-Strong correlation between radar backscatter and trunk biomass. -HV polarization is most sensitive to trunk biomass. -Phase difference between HH and VV correlated to diameter at breast height (dbh).
Treuhaft et al., 2004	N/A	Signal/noise modeling	InSAR (P, L,C-band)	-Forest biomass more accurately determined by InSAR coherence and phase than by backscatter. -Biophysical properties of vegetation are best determined by data fusion with InSAR.
Solberg et al., 2010	Norway spruce, Scots pine, and birch	Regression analysis	InSAR (X-band)	-Relationship between biomass and InSAR height is linear and no apparent saturation detected.
LiDAR				
Lefsky et al., 2002	Mixed softwood	Regression analysis	LiDAR (Waveform)	-Single regression equation can be used to relate LiDAR derived canopy structure to AGB.
Næsset and Gobakken, 2008	Norway spruce, Scotch pine	Regression analysis	LiDAR (Discrete-return)	-Below ground biomass and AGB can be estimated from LiDAR data in boreal forest with good accuracy.
Asner et al., 2010	Tropical rainforest	Sampling and Regression analysis	LiDAR (Discrete-return	-Use of LiDAR as sampling tool to support broad-scale biomass assessment in Peru.

Table 1.2 Cont'd.

Authors	Vegetation Types	Methods	Data Sources	Key Findings
SAR/INSAR & LiDAR Integration				
Slatton et al., 2001	N/A	Data fusion using multi-scale filter	LiDAR (Disrete-return) and InSAR (C-band)	-Combining physical modeling with multi-scale estimation can significantly improve estimates of tree heights over large areas
Simard et al., 2006	Mangrove	Empirical calibration of InSAR heights using LiDAR	LiDAR (Discrete-return) and C and X-band InSAR	-Biomass can be accurately estimated using LiDAR measurements to calibrate InSAR mean heights to top of canopy heights.
Hyde et al., 2007	Ponderosa pine	Integration using regression analysis	LiDAR (Discrete-return, UHF and VHF SAR, and X, P-band InSAR	-LiDAR more accurate in predicting forest biomass compared to SAR. -LiDAR derived mean height is highly correlated to biomass. -Addition of SAR and InSAR variables only slightly improved biomass estimates.
Sun and Ranson, 2009	Mixed hardwood and softwood	Correlation of LiDAR derived biomass with SAR data	LiDAR (Waveform) and SAR (L-band)	-SAR data has the ability to extend biomass estimates to other forested areas, using collocated biomass samples derived from LiDAR.
Mitchard et al., 2012	Savanna, low biomass, and tropical forest	Integration of biomass estimates with SAR classification.	LiDAR (waveform) and SAR (L-band)	-Combining SAR derived land cover with accurate biomass estimates from LiDAR is a potential method to overcome challenges of high biomass and cloud cover.

1.5 Research Objectives

The objective of the research presented in this thesis was to investigate different methods of integrating LiDAR and SAR data to support forest biomass estimation and ultimately, carbon stock assessment. The rationale was to use the precision and accuracy of LiDAR measurements to calibrate and enhance SAR measurements. The chapters in this thesis address the varying spatial scales at which forest characterization and forest biomass can be measured. It begins at

the local scale with an analysis of forest biomass at the plot-level then scales-up to the regional scale with a quantification of forest biomass for a larger area.

To support the research objective, two specific questions were posed:

1. Can LiDAR data, in combination with SAR data, provide more accurate estimates of forest biomass, and individual biomass components, compared to any one technology?

2. How can SAR data be used to extend biomass estimates over large areas using samples of LiDAR data, and at what accuracy?

Chapter 2 describes the study area, including the regional climate, vegetation communities, and the disturbance processes within the area. In additional, this chapter provides a detailed description of the various remote sensing datasets and field plots used throughout this thesis.

Chapter 3 examines the correlations between forest biomass, and biomass components, and LiDAR and SAR data to determine the combined parameters that offer the best relationship to estimate forest biomass. Field measured biomass quantities were first related to a series of LiDAR metrics and radar variables separately to understand individual correlations. LiDAR metrics and radar variables were then combined to assess the relative contribution of each data source.

Chapter 4 tests and demonstrates three data integration methods for producing spatially explicit biomass products suitable for application over a range of environments. Three geostatistical approaches were used to extend accurate biomass transects. These sampled transects were derived from plot-level and LiDAR data, and were extended over a larger area through the integration of wall-to-wall radar data.

Finally, chapter 5 discusses the overall findings, conclusions, and implications of this work, and makes recommendations for future research.

2. STUDY AREA AND DATA SOURCES[1]

2.1 Site Description

The study area is an intensively managed forest dominated by Douglas-fir (*Pseudotsuga menziesii* (Mirb.) Franco) and western red cedar (*Thuja plicata* Donn ex D. Don) located on Vancouver Island, British Columbia, Canada. The area covers a 5 km by 5 km area around Oyster River (UTM Zone 10, NAD83: Upper left 329450E, 5531300N; Lower right 337550E, 5523500N), with a mean elevation of 240 m (range of 120 m to 460 m) above sea level (Figure 2.1). The site consists of predominately second-growth coniferous forest of 70% Douglas-fir, 17% western red cedar, 3% western hemlock (*Tsuga heterophylla* (Raf.) Sarg.), and 10% red alder (*Alnus rubra* Bong.). It is highly productive compared to most other places in Canada, with rotation cycles as short as 60 years (Morgenstern et al., 2004). The density of established stands on the site ranges from 350 to 1200 stem ha^{-1}, with tree height ranging between 10.0 and 35.0 m and average diameter at breast height (dbh) between 12.0 cm and 31.2 cm (Tsui et al., 2012). The forest is the result of harvesting of the original forest from 1920 to 1950. Much of the area did not regenerate naturally (Goodwin, 1937) and, as a result, some of the area was planted starting in the late 1940s, with second growth harvesting and subsequent planting beginning in 1989. The harvesting history has resulted in a patchwork of second growth stands at different successional stages. The site is located within the dry maritime Coastal Western Hemlock biogeoclimatic subzone (CWHxm), of the biogeoclimatic ecosystem classification (BEC) system of British Columbia. This subzone is characterized by cool summers and mild winters with mean annual precipitation of 1,500 mm and a mean annual temperature of 9.1 ^{0}C (Meidinger

[1] A version of this chapter has been published. Tsui, O.W., Coops, N.C., Wulder, M.A., Marshall, P.L., and McCardle, A., (2012). Using Multi-frequency radar and discrete return LIDAR measurements to estimate aboveground biomass in a coastal temperate forest. ISPRS Journal of Photogrammetry and Remote Sensing, 69, 121-133.

and Pojar, 1991). A large portion of the forest was commercially harvested in the 2011 winter and replanted during the 2011 spring.

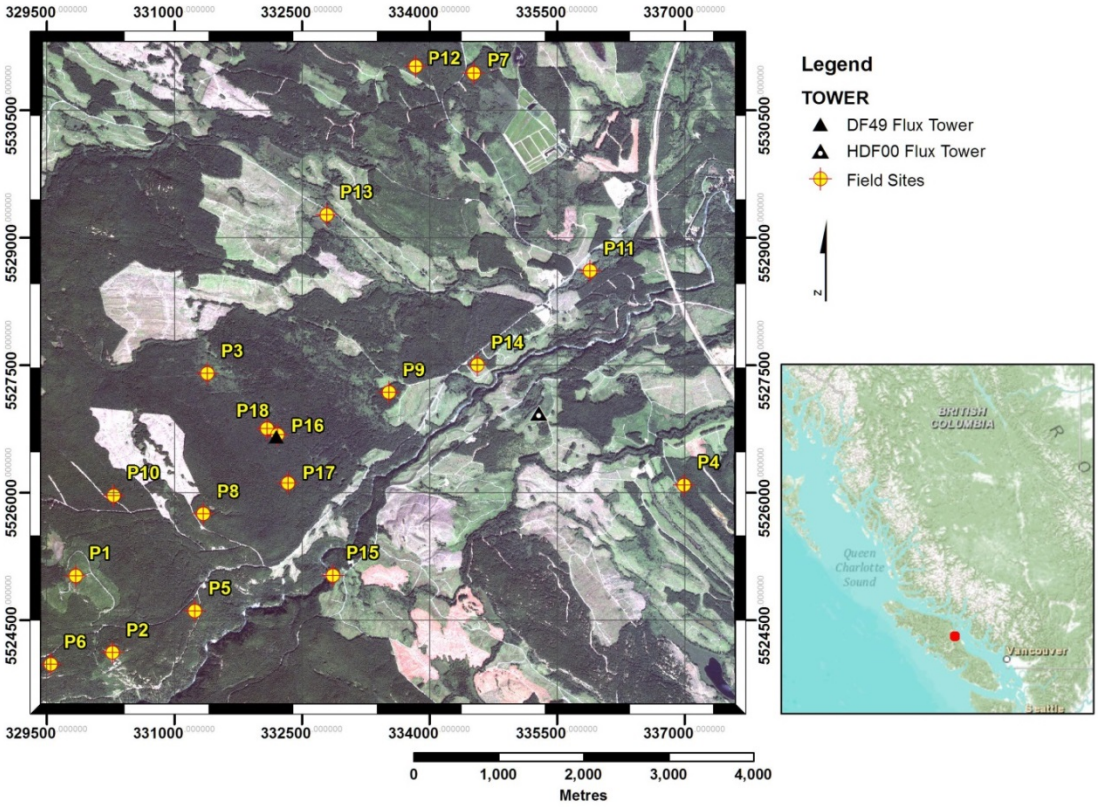

Figure 2.1 Overview of the Oyster River study site and field plot locations.

2.2 Data Descriptions

2.2.1 Plot selection and inventory measurements

Field measurements on seven plots established in 2005 and 2008 were obtained. Complete descriptions of these stands and plot measurements were provided by Coops et al. (2007) and Hilker et al. (2010), respectively for the two measurement dates. An additional 11 stands were selected and visited by field crews from July to September 2010, to capture species composition and age class variability at the study site (Table 2.1). Forest inventory data (derived from 1996 aerial photography and updated in 1999) were provided by the license holders, TimberWest Forest Corp. and Island Timberlands, and were used to support field plot selection. A high

spatial resolution optical image from the QuickBird satellite, acquired August 14th, 2008, was also used. 30 m x 30 m fixed-area square plots were positioned and located using differential GPS (dGPS) for each of these stands. All trees, greater than 10 cm dbh, within the plot were measured for dbh, height, height to the base of the live crown, and species.

2.2.2 Radar data

To investigate the sensitivity of multi-frequency radars, five radar images were acquired: three Fine Beam Dual polarization (FBD) images acquired by the Phased Array type L-band Synthetic Aperture Radar (PALSAR) instrument on the Advanced Land Observing Satellite (ALOS), and two RADARSAT-2 Quad-pol Fine Beam images in single look complex (SLC) format (Table 2.2). The PALSAR sensor, is a fully polarimetric L-band sensor able to operate in either single polarization (HH or VV), dual polarization (HH+HV or VV+VH), or quad-pol mode. The nominal ground resolution for single and dual mode is approximately 10m to 20m, respectively, and 30m for the quad-pol mode. PALSAR's observation strategy provides spatially and temporally consistent regional scale data through the limitation of its operational modes, e.g., fixed incidence angles (34.3^{o}), polarisations (single-pol and dual-pol), and ascending passes (Rosenqvist et al., 2004).

RADARSAT-2 is a fully polarimetric C-band SAR satellite with multiple imaging modes ranging from Spotlight to ScanSAR mode, with nominal ground resolutions of 1m to 100m. Information on the utilization of RADARSAT-2 is given by Van der Sanden (2004). Figure 2.2 presents a colour composite of the L-band and C-band images over the study site in 2009 and 2010 respectively. Different polarizations are used to color code the image: RGB (HH, HV and a ratio of HH and HV for the L-band image, and HH, HV, and VV for the C-band image). Cut blocks and clearings are clearly visible in both radar images; however, younger stands and regenerating stands are less evident in the RADARSAT-2 image.

Table 2.1 Summary of field site characteristics, field measurements, and derived structural metrics per 30 m x 30 m plot.

Plot ID	% DF[a]	% RA[b]	% WRC[c]	% WH[d]	Mean Height (m)	STD Height (m)	Mean DBH (cm)	Tree Density (trees ha^{-1})	Total Basal Area (m^2 ha^{-1})	Vegetation Surface Area / Veg. Volume	Plot Description
1	52.5			33.8	12.3	2.1	12.0	3511	5.1	33.3	Regenerating mixed stand
2	67.9			32.1	18.9	4.1	12.9	1200	7.7	31.0	Regenerating mixed stand
3		84.3		15.6	20.0	4.4	24.9	356	18.2	16.1	Regenerating pure stand
4	100.0				18.1	2.8	17.5	733	18.4	22.9	Young pure stand
5	46.4		25.0	28.5	19.6	7.2	19.2	622	21.0	20.8	Young mixed stand
6	11.8		67.7	20.3	20.7	8.6	24.2	467	25.8	16.5	Young mixed stand
7	97.2			2.7	28.9	6.5	27.4	355	23.2	14.6	Young nearly pure stand
8	41.4	2.9	54.3	1.4	22.6	6.3	21.8	722	30.5	18.3	Young mixed stand
9	61.7		19.1	19.1	27.1	5.7	27.1	488	29.1	14.8	Young mixed stand
10	19.6		58.9	21.4	26.4	7.7	26.4	522	34.0	15.2	Young mixed stand
11	39.6	58.6		1.7	16.9	6.5	21.8	950	33.9	18.3	Young mixed stand
12	98.1			1.8	28.7	4.7	26.9	589	35.3	14.9	Young nearly pure stand
13	14.8	85.1			20.7	6.5	27.7	700	46.4	14.4	Mature mixed stand
14	80.8		19.1		20.9.	4.3	20.6	1325	49.3	19.4	Mature mixed stand

[a]DF = Douglas-fir
[b]RA = red alder
[c]WRC = western red cedar
[d]WH = western hemlock

Table 2.1 Cont'd

Plot ID	% DF[a]	% RA[b]	% WRC[c]	% WH[d]	Mean Height (m)	STD Height (m)	Mean DBH (cm)	Tree Density (trees ha^{-1})	Total Basal Area (m^2 ha^{-1})	Vegetation Surface Area / Veg. Volume	Plot Description
15	80.4	9.9	9.6		26.1	4.9	27.7	575	38.8	14.4	Mature mixed stand
16	81.2		15.0	3.7	25.2	7.9	25.7	855	60.6	23.2	Mature mixed stand
17	55.8		36.3	5.1	23.5	10.0	27.7	866	76.3	14.4	Mature mixed stand
18	81.9		18.1		26.5	6.3	31.2	556	79.3	12.8	Mature mixed stand

[a]DF = Douglas-fir
[b]RA = red alder
[c]WRC = western red cedar
[d]WH = western hemlock

Table 2.2 Radar data sets in terms of products type, acquisition dates and image configurations. Complex pairs used to calculate InSAR coherence are denoted by * and †.

ID	SAR Sensor	Product	Acquisition Date	Incidence Angle (Deg)	Polarisations	Ground Resolution (m)
1	PALSAR	FBD	30-Aug-2008	34.3	HH+HV	~20
2*		FBD	02-Sep-2009	34.3	HH+HV	~20
3*		FBD	18-Jul-2009	34.3	HH+HV	~20
4†	RADARSAT-2	Fine-Quad	07-Aug-2010	39.2	HH+HV+VH+VV	~8
5†		Fine-Quad	31-Aug-2010	39.2	HH+HV+VH+VV	~8

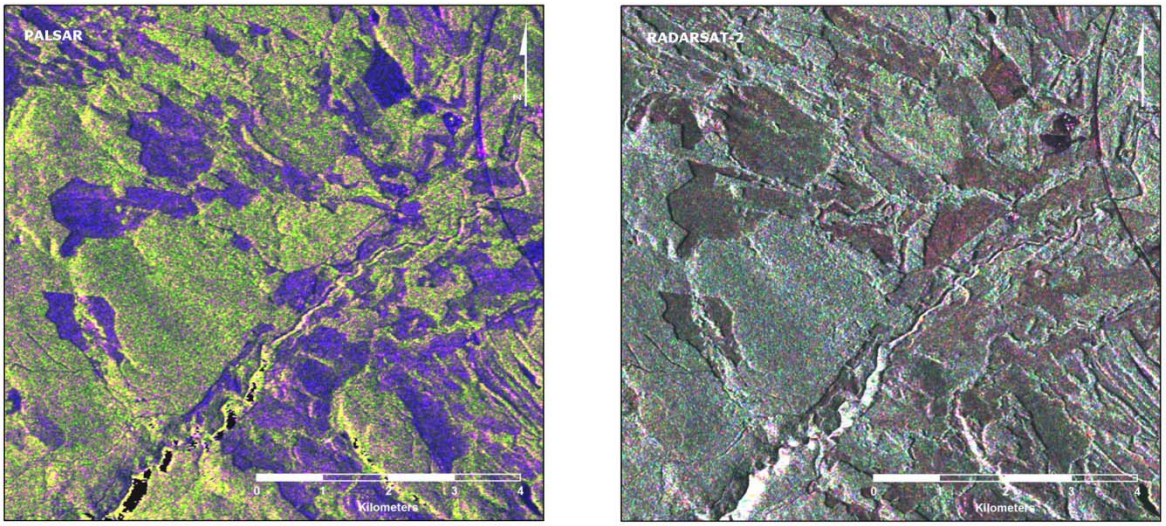

Figure 2.2 L- and C-band colour composites of the Oyster River study site. Red, green, and blue are used for coding HH, HV and a ratio of HH and HV polarizations, for the L-band image, and for coding HH, HV, and VV for the C-band image. The images cover approximately 8 km by 8 km with azimuth direction south to north with the look direction towards the right (east).

2.2.3 Airborne LiDAR data

Airborne discrete-return LiDAR data was acquired on 14 August 2008, using a Leica ALS50-II at a mean flying altitude of 2,303m. The sensor had a 150 kHz pulse rate, recording up to four returns per laser pulse. Based on the pulse frequency, lowest sustainable flight speed, altitude,

and when both ground and non-ground returns were considered, the data had an average point spacing of 0.52 m and an average point density of 3.74 points m^{-2}. These specifications are considered suitable to obtain detailed stand-level structural measurements. Separation of ground and non-ground (canopy) returns was completed using Terrascan v4.006 (Terrasolid, Helsinki, Finland), which employs a series of iterative algorithms that combine filtering and thresholding methods (Kraus and Pfeifer, 1998). After final processing, the bald ground density was between 0.4 points m^{-2} and 1.0 points m^{-2} and the non-ground density was 0.7 points m^{-2}. For additional information on the acquisition parameters of the scanning laser data set, please refer to Hilker et al. (2010).

3. RADAR AND LIDAR OBSERVATIONS TO ESTIMATE ABOVEGROUND BIOMASS AND BIOMASS COMPONENTS [2]

3.1 Introduction

Forest lands in coastal British Columbia are highly productive compared to most of Canada, valued for timber and biodiversity, with biomass levels that are comparable to productive tropical forests. Forest resources have historically been managed primarily for economic value (i.e., timber production); however, current sustainable forest management practices aim to provide a broader range of goods and services over the long term (Siry et al., 2005). Gathering data and reporting on the extent, quantity, composition, and condition of forest resources has traditionally been completed using forest inventories (Kangas et al., 2006). These inventories then form the basis upon which forest management decisions are made, either at the operational level (e.g., planning of silvicultural activities), or strategic level (e.g., forest management plans) (Wulder et al., 2008).

Forest biomass can be sub-divided into its components such as wood, bark, branch, and foliage (more generally the crown and stem), which can provide additional information for ecosystem management. For timber supply needs, merchantable stem volume is of importance, with relationships between stem and non-stem biomass components established (i.e., biomass expansion factors) enabling estimation of biomass (Lambert et al., 2005). Further estimates of biomass components, such as crown biomass, can aid in fuel load assessments and fire management strategies. Canopy fuel characteristics are the most important variables in predicting fire hazard and behavior, making predictions of canopy biomass important for many wildfire models (Saatchi et al., 2007).

[2] A version of this chapter has been published. Tsui, O.W., Coops, N.C., Wulder, M.A., Marshall, P.L., and McCardle, A., (2012). Using Multi-frequency radar and discrete return LIDAR measurements to estimate aboveground biomass in a coastal temperate forest. ISPRS Journal of Photogrammetry and Remote Sensing, 69, 121-133.

Combining information from multiple sensors, or data integration, can be an optimal strategy to characterize forest land and provide information on forest biomass components. Investigations into data integration have yielded promising results when estimating forest structural characteristics. Hudak et al. (2002) combined regression and co-kriging models from multi-spectral and LiDAR data to estimate forest canopy height at un-sampled locations and found that an integrated modeling approach was suitable for estimating canopy height. When investigating the integration of Landsat TM data with polarimetric multi-frequency radar, Moghaddam et al. (2002) found that accuracy in foliage mass estimates were notably improved. Wulder et al., (2007) showed the integration of profiling LiDAR and optical remotely sensed imagery provides improved characterization of forest canopy attributes and change dynamics over a large area of the boreal forest in western Canada.

The objective of this chapter was to investigate the relationships between forest biomass, and its components, across a range of structural age classes, with small-footprint discrete return LiDAR and several C- and L-band radar variables (i.e., backscatter, polarimetry, and interferometric coherence). High correlation between biomass components (e.g. crown biomass) and shorter wavelength radars was expected given the predominate scatterer at these frequencies are branches (Imhoff, 1995b); therefore, the rationale was to examine the additional information provided by C and L-band to determine the combined LiDAR and radar parameters that offer the best relationship in estimating forest biomass and biomass components. This objective was accomplished by calculating biomass and biomass components values using species-specific allometric equations. These quantities were first related to a series of LiDAR metrics and radar variables separately, and then in combination. Multiple regression analysis was then used to assess the relative contribution of each radar variable to a LiDAR derived biomass model providing to obtain the best estimates.

3.1.1 Radar remote sensing background

Studies by Le Toan et al. (1992) and Dobson et al. (1992), demonstrated the response of radar backscatter interactions for various experimental forests stands using experimental airborne SAR sensors at the time. Gaveau et al. (2003) studied InSAR coherence, derived from ERS-1 and ERS-2, to help differentiate four categories of growing stock volume for an area in Central Siberia. Thiel et al. (2009) studied the feasibility of summer backscatter intensities and winter coherence to operationally delineate forest and non-forest land cover. Some studies in the use of SAR for forest characterization have also focused on the relative phase information (i.e. the shift from horizontal or vertical in the transmitted microwave compared to the received microwave signal) in polarimetric data. A review by Treuhaft et al. (2004), suggested that the added information provided by the phase information (InSAR coherence and InSAR heights) for forest monitoring showed promise especially with the fusion with optical remotely sensed data. Availability of commercial SAR satellites with full polarimetric capabilities, and new processing and investigation techniques have led to attempts to address limitations of earlier technologies (Cloude and Papathanassiou, 1998). A complete overview of forest biomass estimation through radar is provided by Koch (2010). In general, there are two methods to obtain estimates of aboveground biomass, direct and indirect. Direct methods primarily use radar responses (e.g., backscatter, SAR coherence) to establish relationships with forest biomass or forest structure. Indirect methods use radar derived forest structural estimates (e.g., tree heights, or canopy heights obtained through Interferometric SAR – InSAR or Polarimeteric InSAR – Pol-InSAR) to infer forest biomass quantities.

The integration of radar technology with other sources of remotely sensed data, even with the limitation of signal saturation, continues to be actively studied for forest biomass estimation and land use and land cover monitoring, especially for tropical regions where cloud cover hinders the operational effectiveness of optical remote sensing sensors (Zhang et al. 2006).

Although previous studies by (Hyde et al., 2007; Nelson et al., 2007) have investigated the integration of these two data types through the use of co-located datasets and aspatial regression methods, their study focused on airborne radars of longer wavelengths. This chapter aims to investigate the integration of LiDAR and shorter wavelength radars to better understand the potential synergies between these data sources. The wide area potential, frequent collection and cloud-free nature of SAR data suggest high utility.

3.2 Material and Methods

3.2.1 Study site

For a complete study site description, please consult Section 2.1. The study area consists of several flux-tower sites (DF49, HDF11, and HDF00) that are part of the Canadian Carbon Program (CCP) located on Vancouver Island, British Columbia, Canada. DF49 was planted in 1949 and is a mature Douglas fir stand. It was commercially harvested during the 2011 winter and replanted during the 2011 spring. HDF-11 was replanted during the spring of 2011, while HDF00 was harvested and replanted in 2000.

3.2.2 Field based biomass estimates

Produced from national archival plot-level data, Ung et al. (2008) developed consistent biomass equations used by the Canadian Forest Service to model the carbon cycle at the national scale. This study calculated tree biomass and the biomass of tree components (e.g., stem, bark, branch and foliage) using these species specific biomass equations. Aboveground and tree component biomass values were calculated for individual trees within each plot and then summed to obtain a summary of the biomass for each plot. It is important to note that although field-based biomass measurements date back to 2005, only a relatively small increase in forest biomass is anticipated to have occurred between 2005 and 2010. Comparison between the 2008 LiDAR data and the 2004 LiDAR data set described by (Coops et al., 2007), showed an average plot-

level increase in stand height of 1.4 to 2.8 m. This corresponds to a change of approximately ±0.1 to 0.2 Mg ha^{-1} in aboveground biomass. Furthermore, a study conducted by Wulder et al. (2008), also reported a low annual increment in tree growth for this study site. We therefore conclude that only small increases in forest biomass occurred between the date the field-based measurements were collected and the remotely sensed data observations.

The field data collected represented a range of structural stages from regenerating stands with low biomass to mature stands with high biomass Table 2.1. To quantify the differences between plots and obtain a consolidated value, two structural descriptors presented by Imhoff (1995b), vegetation surface area (SA) and vegetation volume (V), were calculated using the size and density of the stem and crown component. For each plot, the stem and crown volume were calculated using mean height, dbh, crown height and crown area and then summed. Surface area for stem components were calculated in a similar fashion, while a bulk density was used to calculate the surface area of the crown component. These individual surface area values were also then summed. The ratio of these two descriptors (SA/V) was then used as a measure of the geometric consolidation of the canopy component within the plot. As presented by Imhoff (1995b), a high SA/V value indicates a more diffuse or less consolidated structural type with many small components having a high surface area, while a low SA/V value indicates a high degree of consolidation with fewer but larger crown components resulting in a lower surface area and the presence of canopy gaps.

3.2.3 LiDAR pre-processing

The LiDAR data were processed using FUSION software (McGaughey, 2009). A series of standard plot-level LiDAR metrics were calculated, e.g., mean first return height, standard deviation, coefficient of variation, percentile of first return heights, percentages of first return above 2m, and percentage of first return above the first return mean height. Table 3.1 provides

a plot-level summary of the various metrics calculated for select field plots representing a range of age and structural classes. Only 15 of the 18 field plots were within the spatial extent of the LiDAR data and these were used in the statistical analysis.

Table 3.1 Summary of plot-level metrics calculated from LiDAR data for selected plots representing various age and structural classes.

Plot ID	H_{mean} (m)	H_{max} (m)	H_{std} (m)	CV (m)	P90th (m)	CC_{2m} (%)	CC_{mean} (%)	Plot Description
3	26.44	39.85	2.33	0.09	28.27	98.38	46.11	Regenerating pure stand
8	22.88	34.65	3.88	0.17	27.75	100.00	52.77	Young mixed stand
9	25.80	35.08	5.51	0.21	30.84	94.39	60.91	Young mixed stand
11	16.42	33.27	4.32	0.26	21.76	99.86	41.86	Young mixed stand
13	19.36	33.00	4.14	0.21	24.78	98.70	51.18	Mature mixed stand
14	17.04	28.61	4.48	0.26	22.87	95.92	48.49	Mature mixed stand
15	25.10	36.83	5.29	0.21	31.32	99.48	53.83	Mature mixed stand
16	27.86	42.38	4.72	0.17	32.88	96.95	53.04	Mature mixed stand
17	27.51	41.79	7.15	0.26	35.31	96.77	57.11	Mature mixed stand
18	28.24	41.20	5.08	0.18	33.80	96.56	52.54	Mature mixed stand

H_{mean} = Mean first return height
H_{max} = Max first return height
H_{std} = Standard deviation of the first return heights
CC_{mean} = Percentage of first returns above first return mean heights
CV = Coefficient of variation of the first return heights
$P90^{th}$ = 90^{th} percentile of the first return heights
CC_{2m} = Percentage of first returns above 2 m

3.2.4 Radar data pre-processing

To reduce speckle, the PALSAR and RADARSAT-2 data were multi-looked using factors of 2 and 8, and factors of 1 and 2 respectively, for range and azimuth directions and then calibrated to obtain SAR backscatter images. The updated calibration factor provided by JAXA was used for absolute calibration of the PALSAR data sets (Shimada et al., 2009). For image geocoding, a

1:20,000 scale Terrain Resource Information Management (TRIM) Digital Elevation Model (DEM), with 25m cell size was used. Radiometric correction, geometric correction and terrain correction of the ALOS-PALSAR and RADARSAT-2 data was performed using the Alaska Satellite Facility (ASF) MapReady software package.

Studies have reported that areas of sloped terrain can induce 2-7 dB dispersion on radar backscatter (Castel et al., 2001). Without radiometric normalization, areas with slopes facing the radar sensor would have higher backscatter than flatter areas, which is problematic when assessing properties of backscatter. Topographic effects were therefore corrected by radiometric normalization of the backscatter coefficient using the method described by Kellndorfer et al. (1998). A simple normalization equation was used, where backscatter coefficients were corrected based on the true local incidence angle instead of the ellipsoidal "flat" surface. To obtain a better representation of the backscatter coefficients for distributed targets (i.e., the forest), a conversion from sigma nought to gamma nought was also applied. This allowed for a normalized radar cross-section where backscatter remained approximately constant for all incidence angles.

3.2.5 Polarimetric processing

The relationships between a feature's physical properties (i.e., shape), and its polarimetric behavior can be interpreted by examining the underlying scattering mechanisms, with scattering processes changing between forest stands of different structural types and ages. Through a target decomposition technique or a means to interpret the scattering matrix, the degree of randomness and the mean scattering mechanism of forest stands can be determined by the entropy and alpha parameters (Cloude and Pottier, 1997). For example, high entropy is assumed to correspond well to high crown biomass (branch and foliage) at shorter wavelengths, given the main scattering mechanisms result from tree branches and smaller

twigs. Therefore, in addition to backscatter intensities of the different polarizations, a target decomposition technique was applied to the PALSAR and RADARSAT-2 data to derive a series of polarimetric parameters. The entropy (H), alpha (α), and anisotropy (A) target decomposition parameters were calculated using PolSARPro provided by the European Space Agency (ESA).

3.2.6 InSAR processing

By measuring the phase difference of an object (e.g., a tree branch) that is observed by an InSAR pair, the degree of correlation (coherence) can be calculated. Typically, as the phase variation increases, mainly caused by random fluctuations (e.g., wind induced movements), coherence decreases within a range from 1 to 0. Vegetation causes coherence to decrease; therefore, in general coherence magnitudes are highest for open areas and decrease for areas of dense vegetation (Rosen et al., 2000). Given these observations high biomass areas should exhibit low coherence and areas of low biomass should have higher coherence. The correlation and the magnitude between two radar images with similar orbit geometries (e.g. InSAR coherence), was calculated using the L- and C-band data sets. The perpendicular baselines for the L- and C-band data sets were 615m and 280m respectively, both of which were suitable for processing and analysis. At 46 and 24 days respectively, the L- and C-band pairs had the shortest (best) possible temporal baselines of an orbiting cycle.

3.2.7 Statistical analysis

Most LiDAR metrics are related to canopy height and are often highly correlated, Li et al. (2008) recommended the selection of specific candidate metrics to reduce redundant information while maintaining biological relevance. A subset of candidate LiDAR metrics was selected for use in further analysis. For the radar data, ground-calculated biomass and all radar-derived variables were plotted to verify key assumptions. Non-linear relationships were noted and a log

transform was applied to all ground based biomass estimates (Rignot et al., 1994). Both predictor variables and plot-level biomass were transformed to their natural logarithms before any analysis was conducted. Linear regression was used to create models of biomass as a function of the response variables using the statistical package R. Metrics were modeled for aboveground, stem and crown biomass for the LiDAR data set in a multiple regression analysis, using the regsubsets function from the Leaps package (Leaps 2009). The regsubsets function performs an "all subsets" regression where all possible variable combinations are considered and the best single (independent) variable model is reported, then the best two-variable model, the best three-variable model, and so on. Akaike's Information Criterion (Akaike, 1973) was employed and parsimony was used to determine the best models.

Linear regression was also used to create models of biomass as a function of all radar variables. Each radar variable was modeled separately using the Linear Model (lm) function and also in combination with other variables including the LiDAR model in a multiple regression analysis.

The adjusted R-squared (adjusted R^2) and relative root mean squared error (i.e., the root mean squared error divided by the mean biomass value – relative RMSE), were used to determine fits for both LiDAR and radar models. Due to the difference in spatial coverage between the LiDAR and radar data sets, three field plots were not available for the LiDAR model.

3.3 Results

3.3.1 Biomass estimates

Ground-based biomass components calculated using field measured heights and DBH are presented in Figure 3.1. Aboveground biomass ranged from 20 Mg ha^{-1} for regenerating stands to 550 Mg ha^{-1} for mature stands. On average 68% of the aboveground biomass of a tree was contained within the stem, 16% in branches, and 8% in bark and foliage.

3.3.2 Regression models

The final LiDAR models explained close to 86% of the variance in the plot-level measurements, with all dependent variables predicted well by the LiDAR canopy height and cover metrics. Table 3.2 provides a summary of the final biomass models. Stem biomass had the highest relationship with the LiDAR data, with an adjusted R^2 of 0.86 and a relative RMSE of 16%.

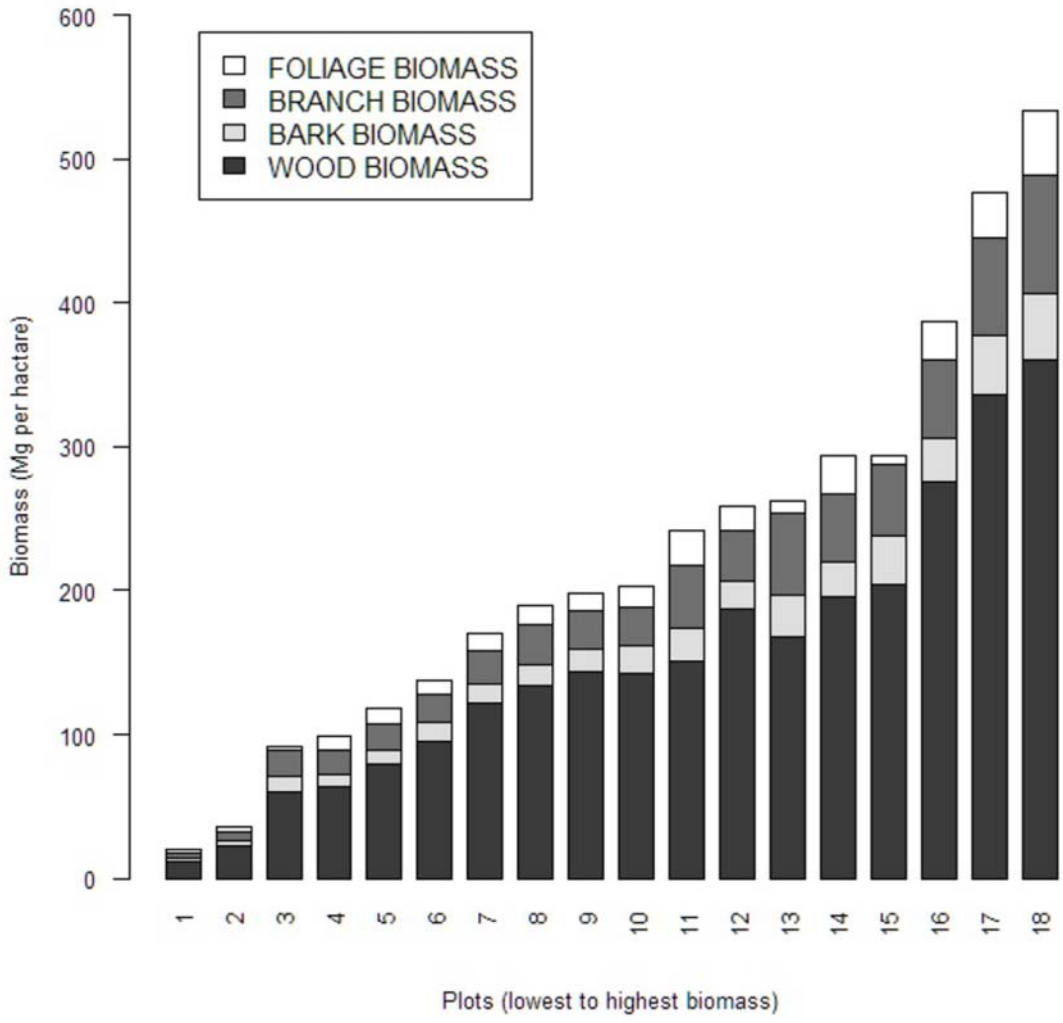

Figure 3.1 Calculated aboveground biomass (Mg ha^{-1}) and individual biomass components per plot as derived by species specific allometric equations published by Ung et al. (2008).

Aboveground biomass showed an adjusted R^2 of 0.82 and a relative RMSE of 18%. Crown biomass showed the lowest relationship with an adjusted R^2 of 0.72 and a relative RMSE of 22%. For aboveground biomass and stem biomass, the mean first return height and percentiles (i.e., 10th and 90th) of first return heights were selected as predictor variables from the subset of candidate LiDAR metrics. For crown biomass, the percentage of first returns above 2m, and 75th and 90th percentiles of first return heights were selected as predictor variables.

Table 3.2 LiDAR biomass models developed from field-measurements and LiDAR canopy height and cover metrics.

	Variables	Adjusted R^2	Model	Root Mean Square Error (Mg ha^{-1})	Relative RMSE (%)
Aboveground Biomass	Lh_{mean} *** Lh_{P10} ** Lh_{P90} ***	0.82	$-7.144 - 12.925x_1 + 2.239x_2 + 14.019x_3$	56.43	17.9
Stem Biomass	Lh_{mean} *** Lh_{P10} *** Lh_{P90} ***	0.86	$-7.965 - 12.997x_1 + 2.281x_2 + 14.218x_3$	40.09	16.4
Crown Biomass	CC_{2m} * Lh_{P90} *** Lh_{P75} ***	0.72	$7.350 - 4.008x_1 + 17.601x_2 - 13.502x_3$	15.41	21.9

In all cases, n= 15
* Variable is significant at $P < 0.05$
** Variable is significant at $0.001 < P < 0.05$
*** Variable is significant at $P < 0.001$

Lh_{mean} = Mean first return height
Lh_{P10} = 10th percentile of the first return heights
Lh_{P75} = 75th percentile of the first return heights
Lh_{P90} = 90th percentile of the first return heights
CC_{2m} = Percentage of first returns above 2 m

Final individual L- and C-band biomass models are summarized in Table 3.3. The relationship between C-band backscatter and biomass was unexpectedly negative, (i.e., decreasing as biomass increased), which differed from most reported results. HH and HV data were weakly correlated with aboveground biomass, while VV polarization was not significantly correlated to biomass or any biomass component. HH polarization was the best predictor variable (adjusted

R^2 = 0.39). C-band coherence values were also negative, decreasing as biomass increased. The coherence magnitudes were quite low, mean ($|\gamma|_{HV}$ = 0.34), however, C-band HV coherence had stronger correlation than HH backscatter and was significantly correlated (adjusted R^2 = 0.71). Saturation of the HV coherence data occurred at approximately 50 to 60 Mg ha^{-1}. Although weak, VV coherence showed significantly higher correlation to forest biomass and the various biomass components than VV backscatter. Polarimetric decomposition variable (entropy and alpha) were not significantly correlated to forest biomass or any biomass component. Consistently, higher correlation with stem biomass and lower correlation with crown biomass was observed for most of the C-band variables.

Table 3.3 Adjusted R-squared values from linear regression of forest biomass and individual L- and C-band radar variables. Most significantly correlated radar variables are represented with a *.

Variable	Aboveground Biomass	Stem Biomass	Crown Biomass
C-Band HH Backscatter	0.39	0.39	0.38
C-Band HV Backscatter	0.21	n/s	0.21
C-Band VV Backscatter	n/s	n/s	n/s
C-Band HH Coherence	0.31	0.32	0.28
C-Band HV Coherence	0.71*	0.71*	0.68*
C-Band VV Coherence	0.57	0.58	0.50
C-Band Entropy	n/s	n/s	n/s
C-Band Alpha	n/s	n/s	n/s
L-Band HH Backscatter	n/s	n/s	n/s
L-Band HV Backscatter	0.61*	0.63*	0.53*
L-Band HH Coherence	0.40	0.41	0.34
L-Band HV Coherence	0.47	0.47	0.44
L-Band Entropy	0.36	0.38	0.29
L-Band Alpha	0.37	0.40	0.30

In all cases, n= 18
Variable is non-significant (n/s), i.e. $p > 0.05$

The L-band backscatter increased linearly with biomass and was generally more highly correlated than the C-band backscatter. L-band HV backscatter was strongly correlated with aboveground biomass. HV polarization was observed to be the best predictor variable (adjusted R^2 = 0.61). Saturation of L-band backscatter was approximately 100-120 Mg ha^{-1}. As with C-band, correlation was slightly stronger for stem biomass than for crown biomass. L-band coherence was also negative, decreasing as biomass increased and did not appear to be any more sensitive to different levels of forest biomass than the backscatter variables. HH and HV coherence were slightly less correlated with biomass than backscatter, with HV coherence as the best predictor variable (adjusted R^2 = 0.47). In contrast to C-band relationships, moderate correlations were observed for the L-band polarimetric parameters (entropy and alpha), with the alpha angle as the best predictor (adjusted R^2 = 0.37).

Modeling forest biomass as a function of both L-band and C-band variables provided improved fits relative to their respective individual values. Five separate models were evaluated, all variables from either L- and C-band; backscatter coefficients from L- and C-band; coherence from L- and C-band; and finally all L- and C-band variables. Significant variables, adjusted R^2, RMSE, and relative RMSE for each model are presented in Table 3.4. High relative RMSE was observed for the individual C-band and L-band models, 53.6% and 44.0% respectively. Combining the L-band and C-band variables provided significant improvement in the predicted values and showed a lower relative RMSE. The L- and C-band coherence model provided the best estimates of forest biomass with a relative RMSE of 35.7% and an adjusted R^2=0.79. The L- and C-band backscatter model had slightly higher relative RMSE of 45.3% compared to the all L-band variable model. Although the all variables model provided a higher adjusted R^2, a higher relative RMSE (39.9%) was observed when compared to the L- and C-band coherence model.

Overall results presented in Figure 3.2, suggest that integrating L-band coherence variables with the best LiDAR-only model showed only a slight increase in relationship with aboveground biomass and stem biomass with an adjusted R^2 = 0.88 and 0.90 respectively. L-band HV coherence was only able to explain an additional 2.4% and 1.2% of the variability in aboveground and stem biomass. No significant improvement was observed for crown biomass using L-band radar.

Table 3.4 All subsets regression biomass models developed from L- and C-band radar variables.

	Variables	Adjusted R^2	Model	Root Mean Square Error (Mg ha^{-1})	Relative RMSE (%)
C-band all variables	C.HH Backscatter *** C.VV Backscatter **	0.76	$4.046 - 0.967x_1 + 1.157x_2$	119.61	53.6
L-band all variables	L.HV Backscatter *** L.HH Backscatter ** L.Entropy **	0.83	$24.892 + 1.728x_1 - 1.432x_2 - 14.882x_3$	98.17	44.0
L- and C–band Backscatter	L.HV Backscatter *** C.HV Backscatter *	0.74	$1.446 + 0.469x_1 - 0.425x_2$	101.07	45.3
L- and C-band Coherence	L.HV Coherence * C.HV Coherence **	0.79	$7.432 - 1.379x_1 - 13.297x_2$	79.79	35.7
All variables	L.HV Coherence * C.HH Backscatter *** C.VV Backscatter **	0.87	$4.159 - 1.534x_1 - 0.786x_2 + 0.899x_3$	89.21	39.9

In all cases, n= 18.

* Variable is significant at $P < 0.05$

** Variable is significant at $0.001 < P < 0.05$

*** Variable is significant at $P < 0.001$

In contrast, integrating C-band backscatter and polarimetric entropy with the LiDAR-only model showed significant improvement ($P < 0.05$) for aboveground biomass, stem and crown biomass with an adjusted $R^2 = 0.94$, 0.95, and 0.89 respectively. Relative RMSE for aboveground biomass, stem and crown biomass were 8.0%, 7.1%, and 11.8% respectively (Table 3.5). C-band HH backscatter was able to explain an additional 8.9% and 6.5% of the variability in aboveground and stem biomass, while C-band polarimetric entropy was able to explain an additional 17.9% of the variability in crown biomass. Predicted vs. observed aboveground biomass were also plotted for all models and presented in Figure 3.3.

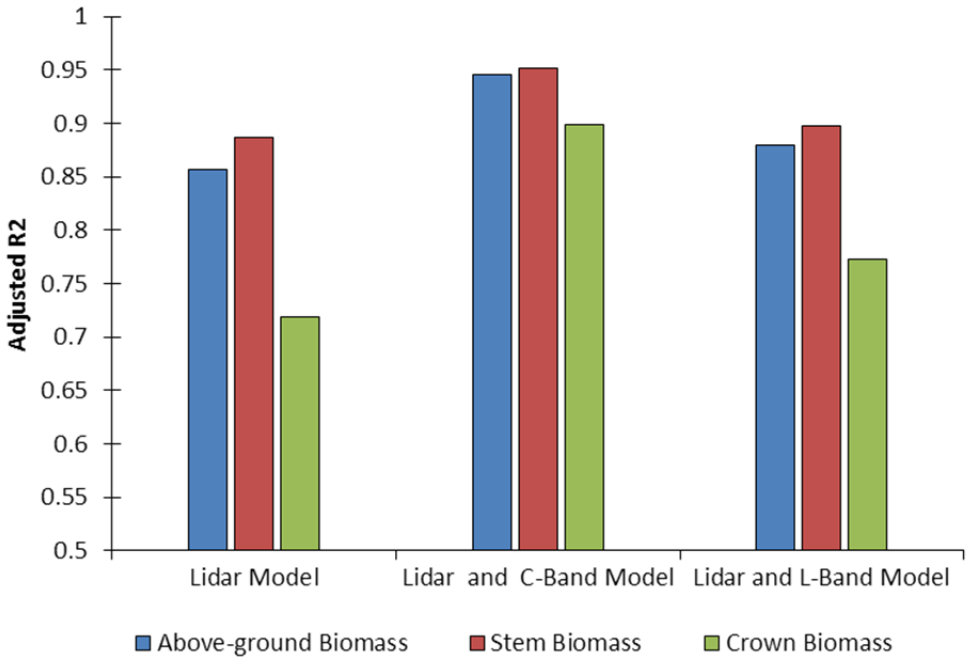

Figure 3.2 Comparison of adjusted R^2 values for the LiDAR-only, LiDAR + C-band, and LiDAR + L-band models. LiDAR + C-band HH backscatter showed the best adjusted R^2 for stem and total biomass, and LiDAR + C-band entropy showed the best adjusted R^2 for crown biomass. LiDAR + L-band HV coherence showed the best adjusted R^2 for both total and component biomass.

Table 3.5 Final biomass models developed from integrating LiDAR and C-band radar for aboveground, stem and crown biomass. Significant variables, adjusted R^2, RMSE and relative RMSE are shown for each biomass model.

	Variables	Adjusted R^2	Model	Root Mean Square Error (Mg ha^{-1})	Relative RMSE (%)
Total Aboveground Biomass	Lh_{mean} *** Lh_{P10} ** Lh_{P90} *** $HH_{c\text{-}band}$*	0.94	$-14.439 + 2.745x_1 - 8.311x_2 + 10.112x_3 - 0.305x_4$	23.64	7.96
Stem Biomass	Lh_{mean} *** Lh_{P10} *** Lh_{P90} *** $HH_{c\text{-}band}$*	0.95	$-14.886 + 2.628x_1 - 8.045x_2 + 10.094x_3 - 0.282_{x4}$	16.40	7.12
Crown Biomass	CC_{2m} * Lh_{P90} *** Lh_{P75} *** $H_{c\text{-}band}$ *	0.89	$-21.164 + 3.153x_1 - 9.373x_2 + 11.116x_3 - 25.126_{x4}$	7.93	11.79

In all cases, n= 15
* Variable is significant at $P < 0.05$
** Variable is significant at $0.001 < P < 0.05$
*** Variable is significant at $P < 0.001$

Lh_{mean} = Mean first return height
Lh_{P10} = 10th percentile of the first return heights
Lh_{P75} = 75th percentile of the first return heights
Lh_{P90} = 90th percentile of the first return heights
CC_{2m} = Percentage of first returns above 2 m
$HH_{c\text{-}band}$ = C-band HH backscatter
$H_{c\text{-}band}$ = C-band polarimetric entropy

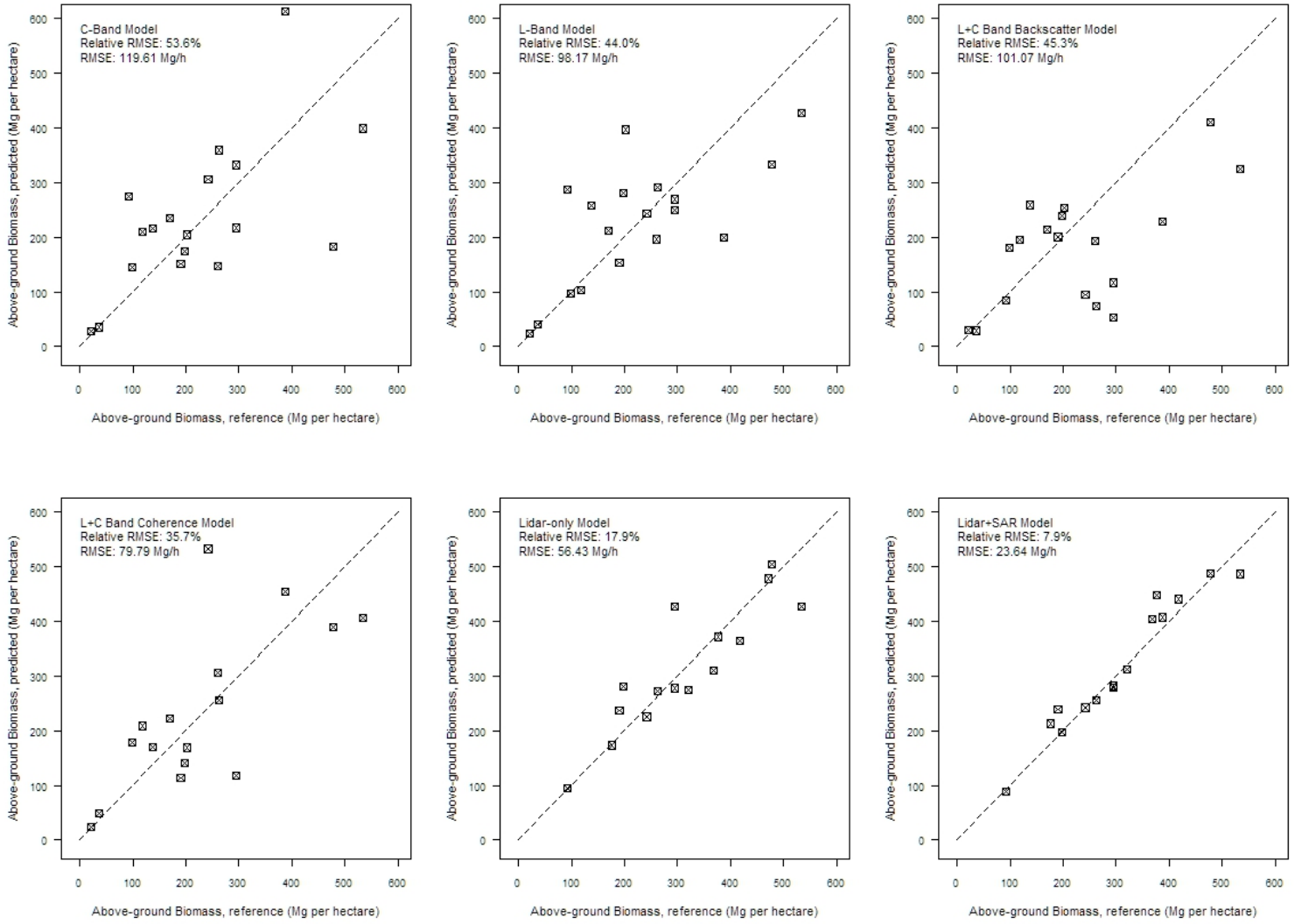

Figure 3.3 Comparison of predicted and observed aboveground biomass for all final C- and L-band radar, LiDAR, and LiDAR + C-band derived models.

3.4 Discussion

3.4.1 LiDAR

It is acknowledged that the total number of plots used in this study was small. Additional work field work could have added more plots and provided additional validation and robustness to the observed relationships. With the noted limitations of the sample size, this study was able to demonstrate the various relationships between forest biomass, and its components, with LiDAR and radar backscatter, polarimetry, and interferometric coherence from both C and L-band radar sensors. It confirmed that discrete-return LiDAR height measurements perform well in determining forest biomass and biomass components. The resulting LiDAR metrics selected in this study, e.g., mean height, 90th percentile, 75th percentile, and the percentage of first returns above 2m were the main variables found to explain the majority of the variation. Overall these selected metrics are consistent with previous LiDAR studies (Hall et al., 2005; Li et al., 2008; Næsset et al., 2005). Since most LiDAR returns result from hits from dominant trees, especially from the outer canopy, distribution of LiDAR return heights is weighted toward the tallest trees (Hall et al., 2005). Therefore the mean and 90th percentile heights likely represent the height of the over-story and the75th percentile and the percentage of first returns above 2m, provides a measure of the spatial variability in canopy heights (Li et al., 2008). For all models the combination of height metrics and canopy cover metrics provides the three dimensional information needed to estimate the different components of forest biomass.

3.4.2 Multi-frequency radar

As for L-band and C-band radar, the use of multi-frequency radar performed better than any single frequency radar with respect to estimates of aboveground biomass. Modeling individual biomass components (stem and crown) with L- or C-band backscatter, coherence, and polarimetric variables did not improve the relationship compared to the aboveground biomass

model. Although combining L- and C-band variables produced a strong correlation with biomass, relative RMSE values were high due to saturation at higher biomass levels. Nonetheless, error levels obtained from this study were within the range of other studies for single-date and multi-temporal data. For example, relative RMSE values for C-band estimates from a number of studies reported by Santoro et al. (2011), ranged from 49.6% to 80.0%, while relative RMSE values from this study ranged from 35.7% to 53.6% for C- and L- band estimates. For polarimetric parameters, specifically entropy and alpha angle, and forest biomass showed moderate correlation. The degree of correlation between L-band entropy and alpha angle is consistent with findings made by Melon et al. (2002), and suggested all polarimetric discriminators in L-band data have similar sensitivity to forest biomass, when compared to backscatter. Therefore their use in forest parameter retrieval (e.g., forest biomass) may not provide additional information.

The dominant scattering within the crown layer can be associated to foliage and branches; therefore, a correlation between crown biomass and C-band variables was expected. The absence of such a response may be a result of the structural components of the stands at the study site. Examining the ratio of vegetation surface area and vegetation volume (SA/V), younger regenerating stands displayed a canopy structure containing many small components, resulting in a high SA/V, while mature stands had lower SA/V indicating a canopy structure with fewer but larger crown components. Direct volume scattering, as described by Le Toan et al. (1992), from the crown surface would be higher in stands with diffuse canopies having many smaller components than stands that have more consolidated, but bigger, components and larger canopy gaps. As a result the structural composition of this study site may provide insight and help explain the observed backscatter response from the C-Band radar.

3.4.3 LiDAR and radar integration

Including a radar variable to the LiDAR biomass model showed a significant improvement in the forest biomass estimates. This improvement is greatest in estimating crown biomass. Given that the relationship between plot-level measurements of canopy height metrics and biomass form the basis of estimating forest biomass, canopy heights may not be good predictors of crown biomass but, as we have seen in this study, are more sensitive to stem biomass. With the dominant scattering process associated with branches, and to some extent foliage, C-band radar appears to provide additional information on the crown components to a LiDAR-only biomass model.

Results from this study, however, differ from others; Hyde et al. (2007) and Nelson et al. (2007) investigated LiDAR and radar synergies to improve forest biomass estimates and both studies present consistent results. LiDAR estimated biomass more accurately and precisely than any of the radar variables used in their studies. The use of both LiDAR and radar jointly did not improve forest biomass estimation in a practical sense, even though the addition of radar variables to their best LiDAR-only model was statistically significant (Nelson et al., 2007). When examining the cross-validated RMSE of both the LiDAR-only and LiDAR-radar models, an improvement of 1.6% (Nelson et al., 2007) and 7.8% (Hyde et al., 2007) in predictive precision was observed. Both studies concluded little practical utility could be gained by combining radar data, considering the cost of acquisition and processing.

For this study site, a Douglas-fir and western red cedar dominated forest, the addition of a radar variable to the LiDAR-only model, improved the results by reducing the relative RMSE of the predicted aboveground, stem, and crown biomass levels by approximately 10%. Even with these improved accuracies previous conclusions regarding cost implications in data acquisition and data processing need to be considered. It is unlikely that the benefits obtained from the

inclusion of radar would justify its addition due to cost. However with the eventual launch of the European Space Agency's Sentinel-1 mission and the Sentinel data policy, promoting full and open access to Sentinel data to all users, inclusion of C-band radar with discrete-return LiDAR for a detailed biomass inventory for small areas should be possible. The mandate of the Group of Earth Observations' Forest Carbon Tracking (GEO-FCT) Task, to facilitate access to time-series SAR and optical satellite data, future integration of these two data sets is also encouraging. Although a detailed biomass inventory for small areas is possible, the high cost associated with wall-to-wall LiDAR data collection hinders its use for biomass assessments for larger areas. Future investigations in LiDAR and radar synergies for wide-area biomass monitoring should be conducted. Sample observations provided by LiDAR transects could be integrated with large area radar coverage through spatial modeling methods (i.e. geo-statistical approach), rather than aspatial regression methods. For example, the known relationship between various radar variables and biomass can be exploited through sample observations provided by LiDAR transects and a co-kriging approach.

4. EVALUATING MULTIVARIATE KRIGING TO ESTIMATE AND MAP ABOVEGROUND BIOMASS. [3]

4.1 Introduction

Forests are important at multiple scales, from providing habitat for animals and non-timber products at local scales (Ahrends et al., 2010) to influencing climate systems and the carbon cycle globally (Lewis et al., 2009). Sequestered carbon in the form of vegetation (i.e, forests) is both large and dynamic. Consequently forests are an important component in mitigating the effects of climate change. However, when forests are cleared and converted to other land types or degraded much of their stored carbon is released into the atmosphere as CO_2. As of 2007 deforestation, including decay and peat fires and drained peat soils, is estimated to account for approximately 18 % of global carbon emissions and is the second largest source of anthropogenic GHG emissions (IPCC, 2007). The IPCC has also shown that the largest source of GHG emissions for most tropical countries is from deforestation and degradation. More damaging is that deforestation and degradation of tropical forests also removes globally important carbon sinks that currently sequester CO_2 from the atmosphere, and which are critical to future climate stabilization (Stephens et al., 2007). Spatially explicit maps of aboveground biomass are essential for quantifying the amount of carbon sequestered in forests, and changes in forest carbon stocks and area.

Frequent observation, demonstrated relationships with biomass, and an all-weather data collection capacity encourage further research with radar and LiDAR data. SAR and InSAR data provide a complimentary match of information with LiDAR data for biomass monitoring (Hyde et al., 2006; Wulder et al., 2012a). In an integrative framework, forest biomass estimates derived from LiDAR data can be used to calibrate (and subsequently validate) the wide area

[3] A version of this chapter has been submitted for publication. Tsui, O.W., Coops, N.C., Wulder, M.A., and Marshall, P.L. 2013. Integrating airborne LIDAR and spaceborne radar via multivariate kriging toestimate above-ground biomass. Remote Sensing of Environment.

observations made by radar. For example Mitchard et al. (2012) combined direct observations of L-band radar, space-borne LiDAR, and ground data to map aboveground biomass for Lopé National Park (LNP) in Gabon, an area of 5,000 km^2. PALSAR backscatter (HH and HV polarization), elevation data, and a radar-derived forest degradation index (RFDI) (e.g. ratio between the HH and HV polsarization) were used to produce an unsupervised vegetation classification consisting of 40 classes for the entire national park. Each vegetation class was then assigned an average biomass value estimated by ground and LiDAR data. The LiDAR data consisted of sample profiles, covering only 17.85 km^2 but which intersected all 40 vegetation classes. They estimated the carbon stock of the LNP to be 173 Mg C ha^{-1}, which was consistent to the field data average of 181 Mg C ha^{-1}. The outcome was a 100 m spatial resolution biomass map for the LNP with an estimated uncertainty of ±25.0%.

LiDAR is sensitive to tree level characteristics and height of tress. In contrast, radar is sensitive to the size and arrangement of structural elements of groups of trees with different levels of penetration resulting in a representation of a mean canopy condition (Sexton et al., 2009; Tsui et al., 2012). Given these known relationships between the LiDAR-derived forest biomass and radar measurements, accuracy in predicted biomass over large areas is expected to improve compared to predictions using SAR data alone. The complimentary information content of LiDAR and radar promotes the investigation of additional analysis options, especially those incorporating spatial inter-relationships. The use of geostatistics is one potential method to integrate these complimentary data sources. Through a LiDAR sampling framework, aboveground biomass predictions can be estimated for un-sampled areas aided by wall-to-wall radar, using multivariate kriging approaches (i.e., co-kriging or regression kriging).

The overall goal of this chapter is to test and demonstrate three spatial integration methods to produce spatially explicit biomass products suitable for application over a range of

environments, including remote or less data rich regions. We propose that samples of airborne LiDAR data, calibrated with field data, can be used in conjunction with space-borne radar data to produce viable wall-to-wall maps of aboveground biomass. In support of this goal, we first provide background and context in geostatistics to fulfill this information need. Secondly, we suggest appropriate data sets and methods, followed by an implementation of the proposed approach. Finally we discuss the implementation opportunities and considerations for these integration methods.

4.1.1 Geostatistics

Geostatistics has become a commonly used technique to estimate variables that vary in space (Curran and Atkinson, 1998). A fundamental difference between geostatistics and classical statistics is the assumption of spatial autocorrelation, which describes the correlation between a value of some variable at one location and nearby values of the same variable. Geostatistics is based on the theory of regionalized variables (Matheron, 1971), which assumes variables are stochastic as opposed to deterministic (Olea, 1977).

Semivariograms estimate the degree of dissimilarity (or variance) between pairs of measurements and provides a concise scale and pattern of the spatial variance (Curran, 1988). Given an array of sample sites, or in the case of remotely senses images, an array of pixels, h units apart and the difference of the variable of interest at these sites, the average semivariance, $\hat{\gamma}(h)$, at lag h is given by (Yates, 1948):

$$\hat{\gamma}(h) = \frac{1}{2N(h)} \sum_{i=1}^{N(h)} [z(x_i) - z(x_{i+h})]^2$$

where x_i are the data locations, h is the distance, N(h) the number of sample sites, and z the data value of interest. One of the main uses of the semivariogram is to allow extrapolation of that

variable to unsampled locations (Journel and Huijbregts, 1978). Therefore to describe the semivariogram and apply it in further analysis, it is necessary to fit a mathematical model to the estimated semivariances (Webster, 1985). The variance that is spatially independent is given by the nugget, the sill provides the maximum semivariance observed from the semivariogram where there is no spatial autocorrelation, and the range represents the lag value where semivariance reaches maximum.

Ordinary kriging, the most common and robust form of kriging (Krige, 1966), is a spatial modeling technique that provides optimal and unbiased estimates of unknown vales from sample data (Curran and Atkinson, 1998). The technique is only appropriate when there is spatial dependence in the data and provides estimates by assigning weights to each sample data point that is in close proximity to the estimate of interest. Key to this process is that the weights are determined from the form of the spatial dependence represented by the semivariogram (Curran and Atkinson, 1998). In this sense, estimation is optimal and unbiased since the variance is minimized and weights are chosen so that they sum to one. The ordinary kriging model estimates a value $\hat{Z}$ at location (S_0) and takes the general form:

$$\hat{Z}(S_0) = \sum_{i=1}^{n} \lambda_i \, Z(S_i)$$

where $Z(S_i)$ are the sampled data values, λ_i are the weights assigned to each sampled data value, and n are the number of neighbouring samples used in the model (Goovaerts, 1997). Given the existence of spatial dependence, sample data closer to the estimate are given more weight because they are more likely to be similar to the unknown value.

Co-kriging extends ordinary kriging to account for one or more variables and is typically more appropriate when the primary variable to be estimated (in this study, forest biomass) is under-

sampled with respect to the secondary variable (in this study, the radar observations) (Curran and Atkinson, 1998). Similar to kriging, estimates are calculated using the autocorrelation of the primary variable; however, co-kriging also exploits the inter-variable correlation of the primary and secondary variable. If the two variables are cross-correlated (i.e., the spatial variability of the primary variable is also correlated with the secondary (auxiliary) variable), this information can be used to make predictions of the primary variable (Bivand et al., 2008). Isotopic co-kriging requires that data for the primary variables and auxiliary variables be measured at all sampling locations. Heterotopic co-kriging requires that each variable be measured on different sets of sample points and where only some of the variables may share common sample locations (Wackernagel, 2003). In cases involving remote sensing data, collocated co-kriging is a particular heterotopic situation and is often used where auxiliary variables are measured at all locations but the primary variable is available at only a few locations. Co-kriging estimates a value $\hat{Z}$ at location (S_0) and takes the general form:

$$\hat{Z}(S_0) = \sum_{i=1}^{n_1} \lambda_i \, Z(S_i) \; + \sum_{j=1}^{n_2} \lambda_j \, Y(S_j)$$

Regression kriging is a hybrid approach that combines either a simple or multiple linear regression model with kriging of the regression residuals (Goovaerts, 1997). The value of a target variable at some location can be modeled as a sum of deterministic and stochastic components. Predictions are modeled in two stages: the first is the deterministic part obtained from regressing the depended variable on auxiliary variables; and the second is the stochastic estimates of the model uncertainty (e.g. regression residuals) obtained through ordinary kriging. Estimates for a value $\hat{Z}_{rk}$ at location (S_0) can be obtained with the following:

$$\hat{Z}_{rk}(S_0) = \hat{m}(S_0) \; + \; \hat{e}(S_0) \; = \sum_{k=0}^{v} \hat{\beta}_k \, q_k(S_0) \; + \sum_{i=1}^{n} \lambda_i(S_0) \, e(S_i)$$

where $\hat{m}(S_0)$ is the fitted deterministic component and $\hat{e}(S_0)$ is the interpolated residual estimate from the ordinary kriging, $\hat{\beta}_k$ are the estimated regression coefficients for v auxiliary variables ($\hat{\beta}_0$ is the estimated intercept), and λ_i are the weights determined by the semivariogram for the regression residuals $e(S_i)$.

4.2 Materials and Methods

4.2.1 Study site

For a complete study site description, please consult Section 2.1.

4.2.2 Data description

4.2.2.1 Biomass map

The spatially explicit predictions of aboveground biomass used as the reference data set for this chapter is presented in Section 3.3.2 and was created from plot-based field data and small-footprint discrete-return LiDAR. The LiDAR data was acquired in August 2008 at a mean flying altitude of 2,303m with a bald Earth density of between 0.4 - 1.0 pts m^{-2} and a non-ground density of 0.7 pts m^{-2}. Standard plot-based derived metrics (e.g., mean first return height, standard deviation, coefficient of variation, percentile of first return heights, percentages of first return above 2m, and percentage of first return above the first return mean height) were computed. Biomass, species and age class variability were determined using 18 fixed area field plots measuring 30 m x 30 m, with all trees greater than 10 cm diameter at breast height within the plot measured for dbh, height, height to the base of the live crown, and species. Aboveground biomass for each tree was calculated using species-specific biomass equations and then summed to obtain plot-level biomass values. The final LiDAR-based biomass model had a root mean squared error (RMSE) of 56.43 Mg ha^{-1}, a relative RMSE of approximately 18%, and an adjusted R^2 of 0.82.

Mapping of the empirical model produced a spatially explicit aboveground biomass image at a spatial resolution of 20 m, which matched the spatial resolution of the coarsest radar co-variable used in this study (Figure 4.1). Final biomass values ranged from 0 to 1100 Mg ha^{-1} with a mean biomass value of 304 Mg ha^{-1}.

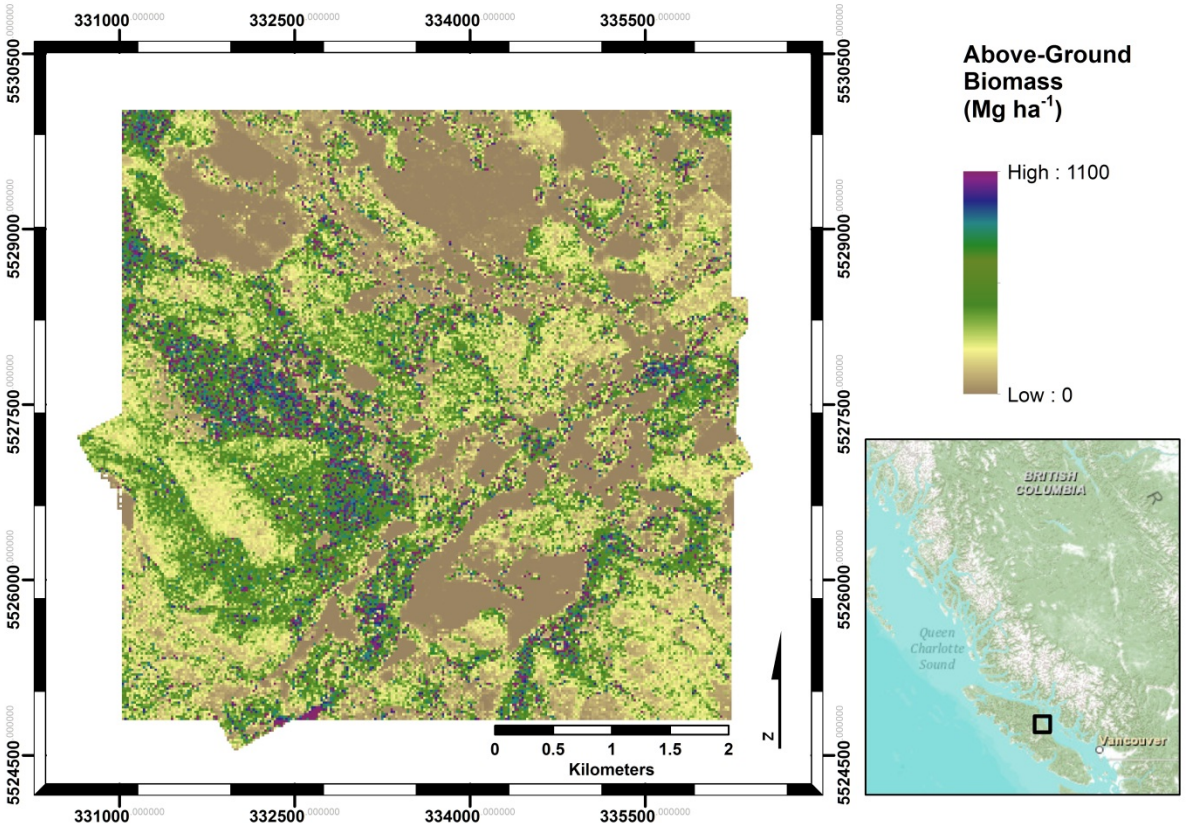

Figure 4.1 Location of study site and aboveground biomass values estimated by discrete-return LiDAR.

4.2.2.2 Radar data

Co-incident to the LiDAR-derived biomass data, five radar images were acquired over the study site. Three Fine Beam Dual polarization (FBD) images acquired by the Phased Array type L-band Synthetic Aperture Radar (PALSAR) instrument on the Advanced Land Observing Satellite (ALOS), and two RADARSAT-2 Quad-pol Fine Beam images. Both data sets were stored in single-look complex (SLC) format (Table 2.2).

PALSAR and RADARSAT-2 SLC data were multi-looked using factors of 2 and 8, and factors of 1 and 2 respectively, for range and azimuth directions and then calibrated to obtain SAR backscatter images. Radiometric, geometric, and terrain correction of the ALOS PALSAR and RADARSAT-2 data were performed using the Alaska Satellite Facility (ASF) MapReady software package. Following radiometric and geometric correction, conversion from sigma nought to gamma nought, which normalizes the radar cross-section where backscatter remains approximately constant for all incidence angles, was completed for an improved representation of backscatter values for distributed targets such as forests. In addition to backscatter images, InSAR coherence magnitudes were also calculated using PALSAR and RADARSAT-2 complex image pairs (i.e. two radar images of similar orbits with amplitude and phase information). By measuring the difference in the phase of the microwave pulses after interacting with an object (e.g., a tree branch), the coherence of the phase can be calculated. As the phase difference or phase shift increases, mainly caused by random fluctuations (e.g., wind induced movements), the coherence decreases within a range from 1 to 0. Since vegetation causes signal coherence to decrease because the exact point of scattering and the travel path of the signals vary between the radar scenes, coherence is highest for open areas and decreases as vegetation increases (Rosen et al., 2000). Lastly, the RADARSAT-2 data were down-sampled to a spatial resolution of 20 m and reduced to a spatial subset equivalent to the extent of the estimate aboveground biomass data set. For a more complete description of the radar processing steps completed, please refer to Section 3.2.

4.2.3 Aboveground biomass sampling

Sample forest biomass values were extracted from the processed biomass data set for the study area. Sampling of these data comprised of both a north-south and east-west continuous transect with each transect line consisting of a data point every 20 m. Transect lines were separated by three distances, either 500 m, 1000 m, or 2000 m with a total number (n) of points of n= 5,540;

n= 3,020; and n = 1,512 respectively (Figure 4.2). The histograms of the three forest biomass data sets exhibited a strong positive skew. Therefore each data set was normalized with a log transformation followed by a normal score transformation before geostatistical analyses were performed. The purpose of the normal score transformation was to obtain a sample distribution closely resembling a standard normal distribution with mean equal to zero and variance equal to one (Olea, 1977). After modeling, all predicted aboveground biomass values were transformed back to the original units (i.e., Mg h^{-1}) before evaluating the accuracy of the various spatial models.

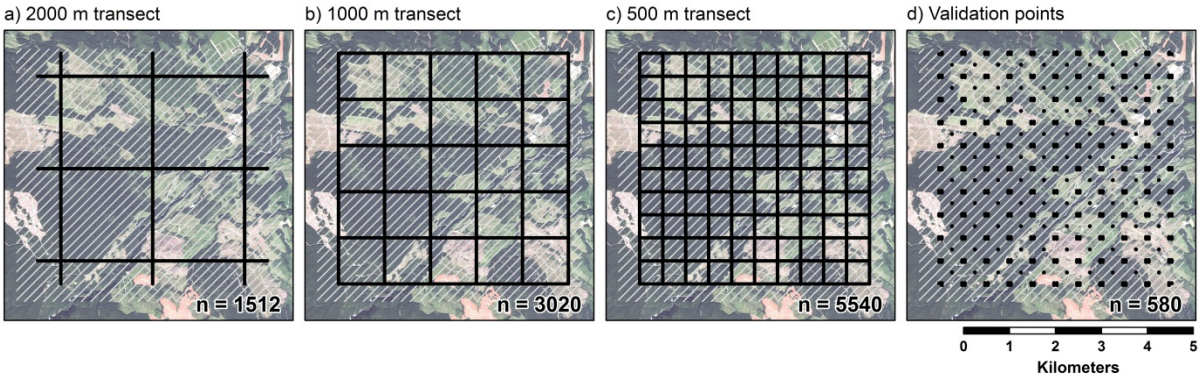

Figure 4.2 Sampling strategies tested and data volumes for each sample forest biomass data set: (a) 2000 m, (b) 1000 m, (c) 500m, and (d) validation points. Shaded grey area represents the extent of the reference LiDAR derived aboveground biomass data set.

4.2.4 Biomass modeling

Aboveground biomass data, derived from LiDAR height measurements, were used as the primary variable, and backscatter intensities and coherence magnitudes from ALOS PALSAR and RADARSAT-2 data were used as wall-to-wall co-variables. The PALSAR and RADARSAT-2 radar backscatter coefficients and coherence magnitudes were also transformed to normalize all datasets prior to use in the estimation processes. Sampling of the primary variable was performed to simulate airborne profiling LiDAR observations. The three multivariate

geostatistical techniques were performed using algorithms found in the GSTAT package designed for the statistical package R (Pebesma, 2004).

For each of the three forest biomass data sets, determining the most suitable mathematical model was assessed by fitting the most common semivariogram models to each of the estimated semivariograms using weighted least squares and evaluating the quality of fit through the residual sum of squares errors. To support the process of predicting biomass values at unsampled locations, wall-to-wall coverage of the secondary variable was included in the kriging process as illustrated in Figure 4.3 for 1000 m transects. For co-kriging a model semivariogram was also calculated for the secondary variable, as well as a cross-semivariogram describing the cross-correlation between the primary and secondary variable. Even though it is possible to model any number of variables, it has been shown that co-kriging results are virtually identical to kriging outputs when spatial correlation between the primary and secondary variable is minimal or absent (Wackernagel, 2003). Given that the correlation between biomass and long wavelength radar is well established (Dobson et al., 1992; Le Toan et al., 1992; Rignot et al., 1994), PALSAR HV-polarization was used as the secondary variable for co-kriging. While developing the three semi-variogram models required for each co-kriging operation, care was taken that each followed the linear model of co-regionalization (Goovaerts, 1997), whereby all models (direct and cross) have the same shape and range, but have different sills and nuggets to ensure that the covariance matrices are always positive.

A three stage process was followed to obtain predictions from regression kriging and regression co-kriging. First, the deterministic part of the predictions was performed by regressing aboveground biomass on the various radar data sets using ordinary least squares to get an estimate of forest biomass for the study area. Secondly, residuals from the ordinary least squares regression were extracted and imported into GSTAT and interpolated across the study

area using ordinary kriging. Lastly, the deterministic and stochastic components were combined together to obtain the final predicted value.

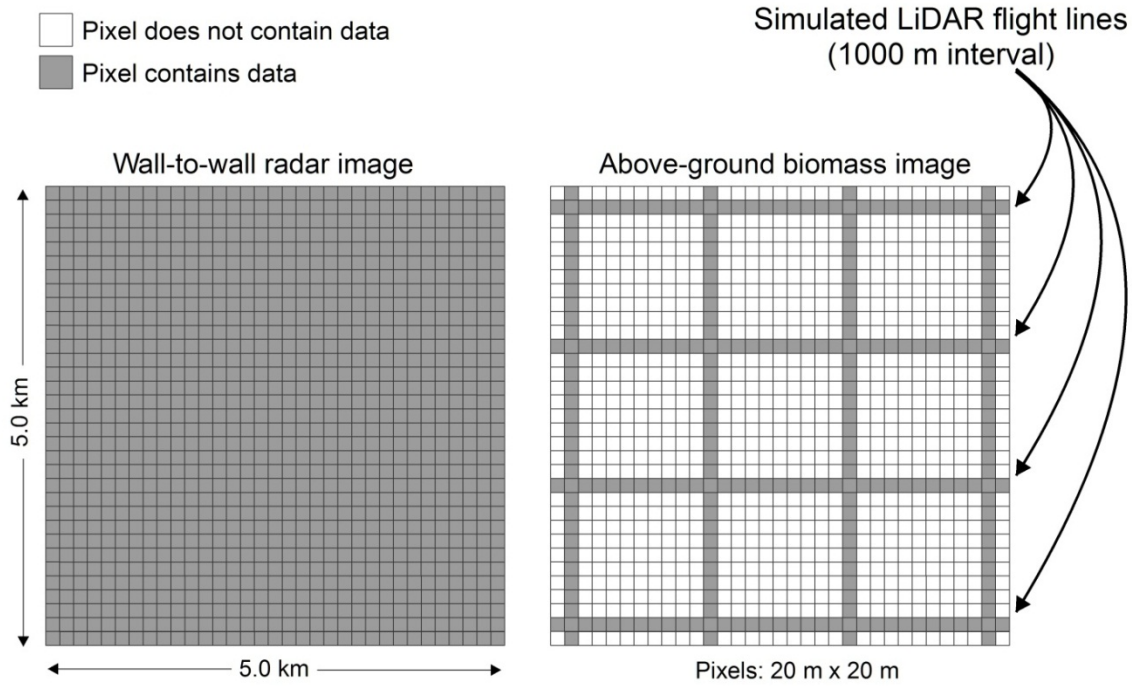

Figure 4.3 Image lattices showing characteristics of the experimental design for multivariate kriging. Aboveground biomass transects simulate airborne profiling LiDAR flight lines at 1000 m intervals.

To determine which radar variables were significant for predicting biomass, a stepwise multiple regression analysis was employed using the regsubsets function from the Leaps package (Leaps 2009) with a significance level of $\alpha = 0.05$. To interpolate the regression residuals for the study area, a model semivariogram was determined following the same procedures outlined for co-kriging. The difference between regression kriging and regression co-kriging primarily lies in the interpolation of the regression residuals. Instead of interpolating the residuals using ordinary kriging, regression co-kriging uses a secondary variable for interpreting the residuals. We selected PALSAR HV backscatter as the secondary variable since this data set had the highest correlation with forest biomass.

4.2.5 Model evaluation

Discrepancies between actual and predicted forest biomass were evaluated based on the validation sample points outlined in Figure 4.2d. The validation data set consisted of 580 forest biomass points extracted from the reference aboveground biomass data set. These points were outside the training data set used in the kriging process. Following (Alsamamra et al., 2009; Meng et al., 2009; Murphy and Katz, 1985) three different and common indices were used:

$$\text{Root Mean Squared Error (RMSE)} = \left[\frac{1}{N}\sum_{n=1}^{N}\left(x_p - x_o\right)^2\right]^{\frac{1}{2}}$$

$$\text{Mean Absolute Error (MAE)} = \frac{1}{N}\sum_{n=1}^{N}\left|x_p - x_o\right|$$

$$\text{Mean Error (ME)} = \frac{1}{N}\sum_{n=1}^{N}\langle x_p - x_o\rangle$$

where N is the size of the validation data set, x_p is the predicted value from the model, and x_o is the observed value from the validation data set. The ME provides an indication of bias in the predictions and it should be close to zero for unbiased methods. The RMSE and MAE measure the average precision of the prediction and provide an indication of how close the predictions are to the observed values. Lastly, paired t-tests were used to compare whether residuals in estimated biomass values differed statistically from one another for each of the transect distances and modeling techniques.

4.3 Results

Semivariograms were generated to analyze and assess the spatial properties of the sampled aboveground biomass transects, biomass residuals, and the radar co-variable data sets. For aboveground biomass all sample intervals showed similar spatial dependence with similar

shape and nugget, partial sill and range parameters. Similar results were found for the biomass residuals and the cross-semivariogram data set. For the aboveground biomass and residual data sets, nugget variance increased as sample interval increased from 500 to 2000 m. The distance where maximum semivariance was observed ranged between 328 to 374 m and 313 to 324 m for the aboveground biomass and residuals, respectively. The cross-semivariograms between the aboveground biomass and the secondary variable showed higher nugget variance and a range distance between 324 to 374 m. Less spatial autocorrelation was observed between the primary and secondary variables, while spatial autocorrelation was evident for aboveground biomass and residual datasets. The Whittle-Matern model had the best fit for all cases and was selected as the theoretical mathematical model for the use in spatial predictions. Example model semivariograms for each variable for the 1000 m sampling interval are provided in Table 4.1 and Figure 4.4.

Point pairs for each variable were graphed to assess if any global trends existed. No obvious trend was found among the individual variables. Anisotropy was also checked in the semivariogram. Similar spatial dependence and semi-variance for all sample intervals at directions of 0, 45, 90, 135, 180, 225, 270, and 315 degrees were found.

Table 4.1 Calculated model semivariograms and cross-semivariogram used in spatial predictions for each variable for the 1000m sampling interval.

Semi-Variogram Model (1000 m)	Model	Nugget	Partial Sill	Range (m)	Kappa
Aboveground Biomass	Whittle-Matern	0.116	0.877	387.493	0.30
Radar co-variable	Whittle-Matern	0.156	0.807	519.417	0.20
Cross-variogram (biomass and radar)	Whittle-Matern	0.397	0.441	328.268	0.40
OLS residuals	Whittle-Matern	0.013	0.801	313.421	0.20

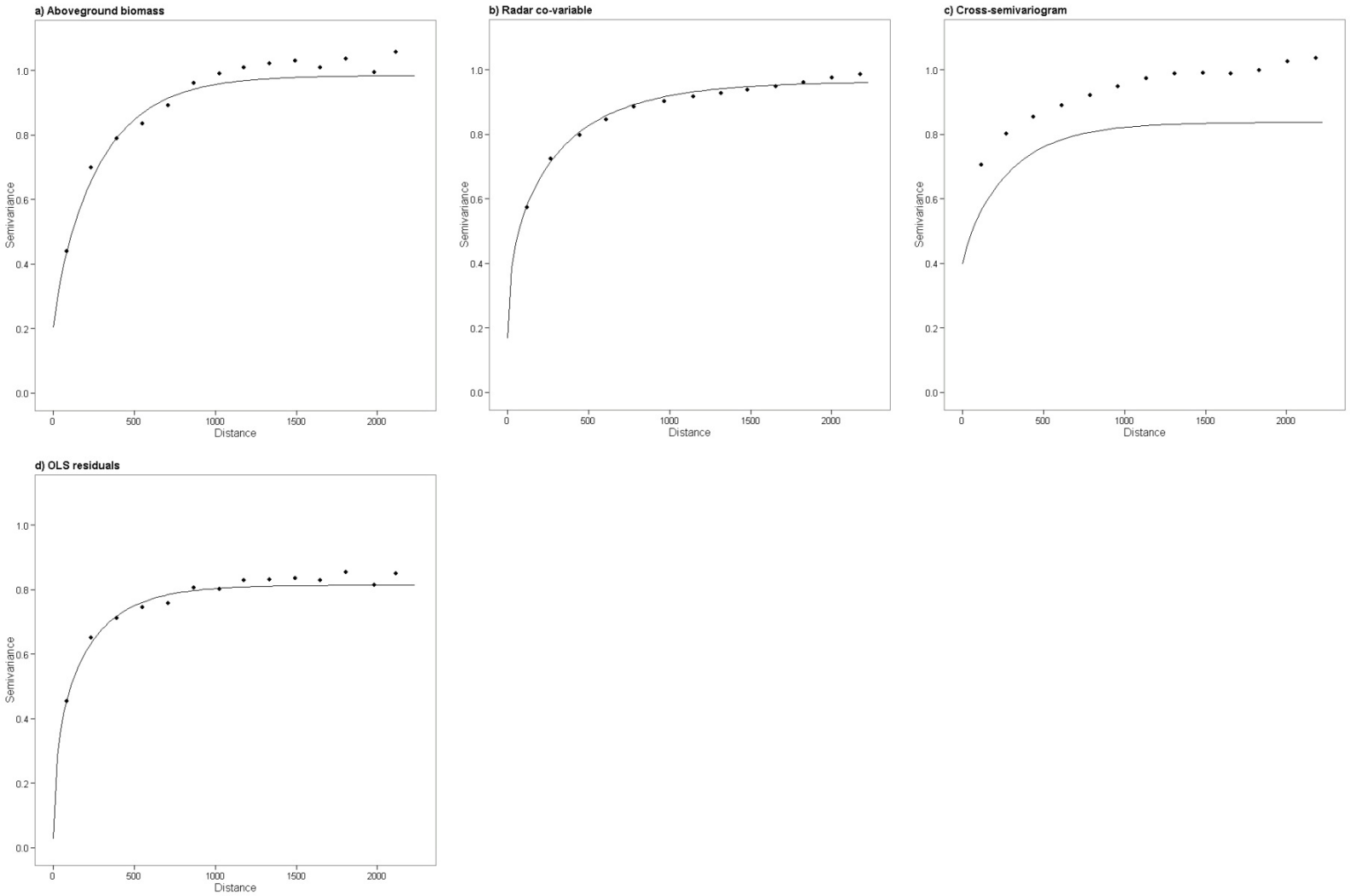

Figure 4.4 Experimental (black points) and model (black line) semivariograms for (a). aboveground biomass, (b) radar co-variable, (c) cross-semivariogram, and (d) OLS residuals for the 1000m sampling interval.

4.3.1 Biomass estimates

Aboveground biomass was underestimated in all cases. Regression kriging at a sample interval of 500 m showed the smallest RMSE and MAE at 203.9 Mg ha^{-1} and 131.6 Mg ha^{-1} respectively. The ME showed an average bias of -14.0 Mg ha^{-1}. Moderate correlation (r = 0.68 and R^2 = 0.46) was observed between predicted and reference aboveground biomass. Predictions using regression co-kriging at a sample interval of 2000 m resulted in the highest RMSE and MAE values at 238.2 Mg ha^{-1} and 164.6 Mg ha^{-1} respectively. Prediction bias also was highest, averaging -37.4 Mg ha^{-1}. Correlation between observed and reference aboveground biomass was also lower at r = 0.52 and R^2 = 0.28 (Table 4.2). Regression kriging generally showed the lowest RMSE, MAE, and ME for all transect distances. As expected, biases in aboveground biomass predictions decreased as transect distances decreased.

Table 4.2 Evaluation of global accuracy for co-kriging, regression kriging, and regression co-kriging based on the validation dataset.

Estimated Aboveground Biomass					
Prediction method and sampling strategy	**RMSE (Mg ha^{-1})**	**Mean absolute error (MAE) (Mg ha^{-1})**	**Mean error (ME) (Mg ha^{-1})**	**Multiple R-squared**	**Pearson's correlation (r)**
Ordinary Co-kriging					
2000 m transect	234.750	162.370	-22.730	0.285	0.533
1000 m transect	219.413	142.802	-34.164	0.383	0.619
500 m transect	205.00	126.758	-24.362	0.458	0.676
Regression kriging					
2000 m transect	237.759	161.951	-35.347	0.255	0.505
1000 m transect	218.729	147.638	-19.523	0.380	0.616
500 m transect	203.900	131.643	-14.007	0.460	0.678
Regression Co-kriging					
2000 m transect	238.228	164.621	-37.349	0.276	0.525
1000 m transect	221.940	152.050	-18.110	0.364	0.604
500 m transect	205.613	134.259	-15.690	0.449	0.670

Histograms of aboveground biomass (Figure 4.5) were used to visualize the accuracy of the predicted values. Deviations of the predicted aboveground biomass histogram from the reference histogram provided further insight into where the majority of the prediction bias occurred. As indicated by ME values, all kriging methods and transect widths underestimated the biomass, with the majority of the deviations occurred at higher biomass levels. Mean predicted aboveground biomass for all methods ranged from 255 to 278 Mg ha^{-1}, a negative deviation of 49 Mg ha^{-1} to 26 Mg ha^{-1} from the mean aboveground biomass of the reference biomass data set. The histograms also showed overestimation of predicted biomass for areas of low biomass values.

Plots of reference and predicted biomass values were also used to compare the different kriging methods and transect widths (Figure 4.6). Improvements can be seen with shorter transect intervals (e.g. larger samples). None of the geostatistical methods predicted aboveground biomass above approximately 1250 Mg ha^{-1} with the exception of co-kriging which had an outlier above 1400 Mg ha^{-1}.

Residuals for aboveground biomass were also graphed for each scenario tested to investigate the distribution of prediction errors (Figure 4.7). Although the range in prediction errors was large for each case, the majority of the deviation between predicted and reference aboveground biomass were between -100 Mg ha^{-1} and 100 Mg ha^{-1}. The variance in residuals decreased as sampling frequency increased. There was not much change in variance among the geostatistical methods within the same sampling frequency. Differences in mean prediction errors were not significant between kriging methods. Co-kriging also showed no significant change in mean predicted errors between sampling distances. While no differences were observed between the 500 and 1000 m for regression kriging and regression co-kriging ($n = 580$; $\alpha = 0.05$; p-value = 0.15 and 0.50 respectively), significant differences were observed between the 1000 m and

2000 m width (n = 580; $\alpha = 0.05$; p-value = 1.2×10^{-3} and 5.7×10^{-4} respectively), and the 500 m and 2000 m width (n = 580; $\alpha = 0.05$; p-value = 3.7×10^{-6} and 7.2×10^{-6} respectively).

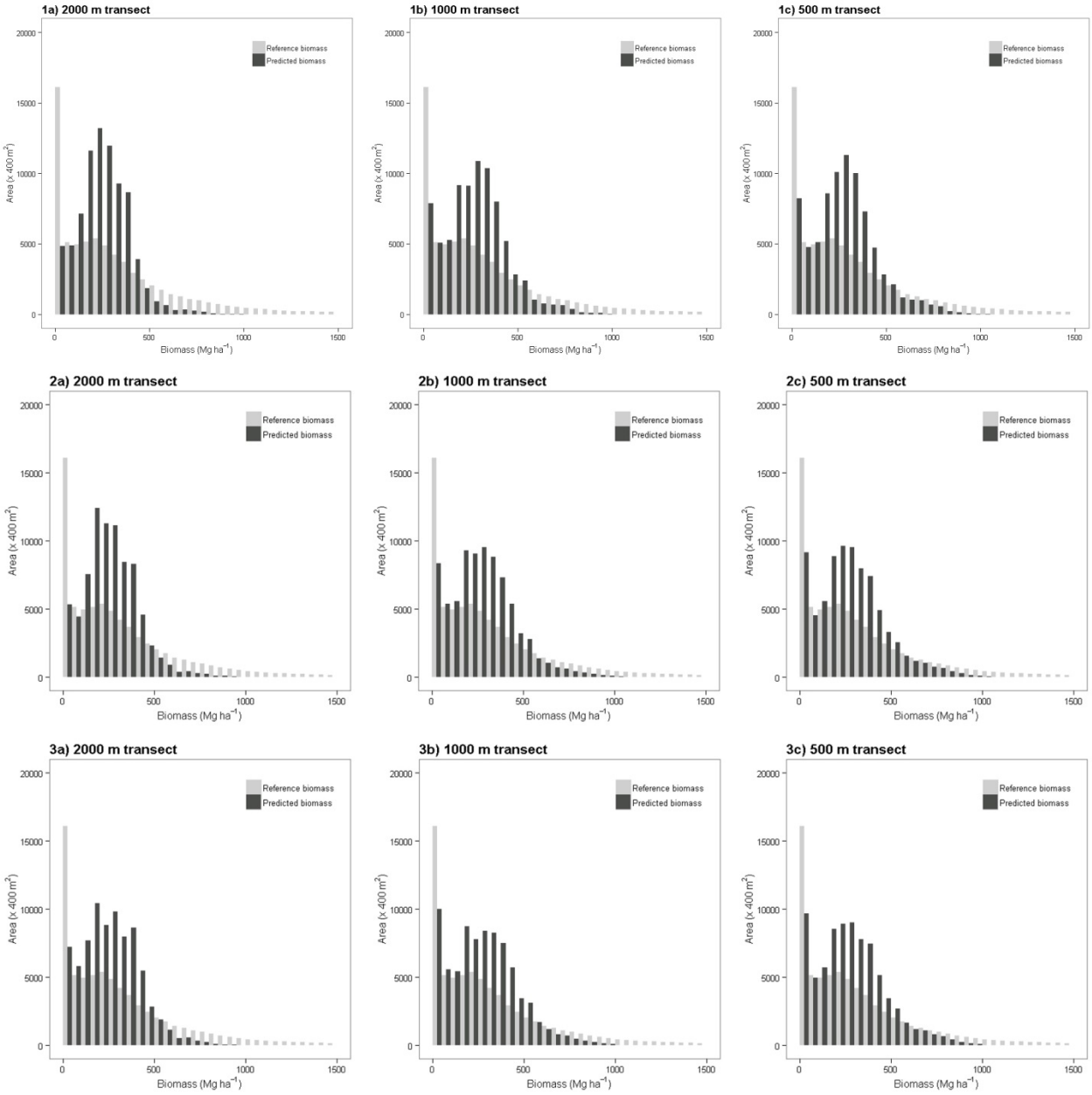

Figure 4.5 Histograms of estimated aboveground biomass values (shaded in black) for all sampling strategies tested. 1. co-kriging (a,b,c); 2. regression kriging (a,b,c); and 3. regression co-kriging (a,b,c). Histogram of reference biomass values provided as reference (shaded in grey, N= 80,025).

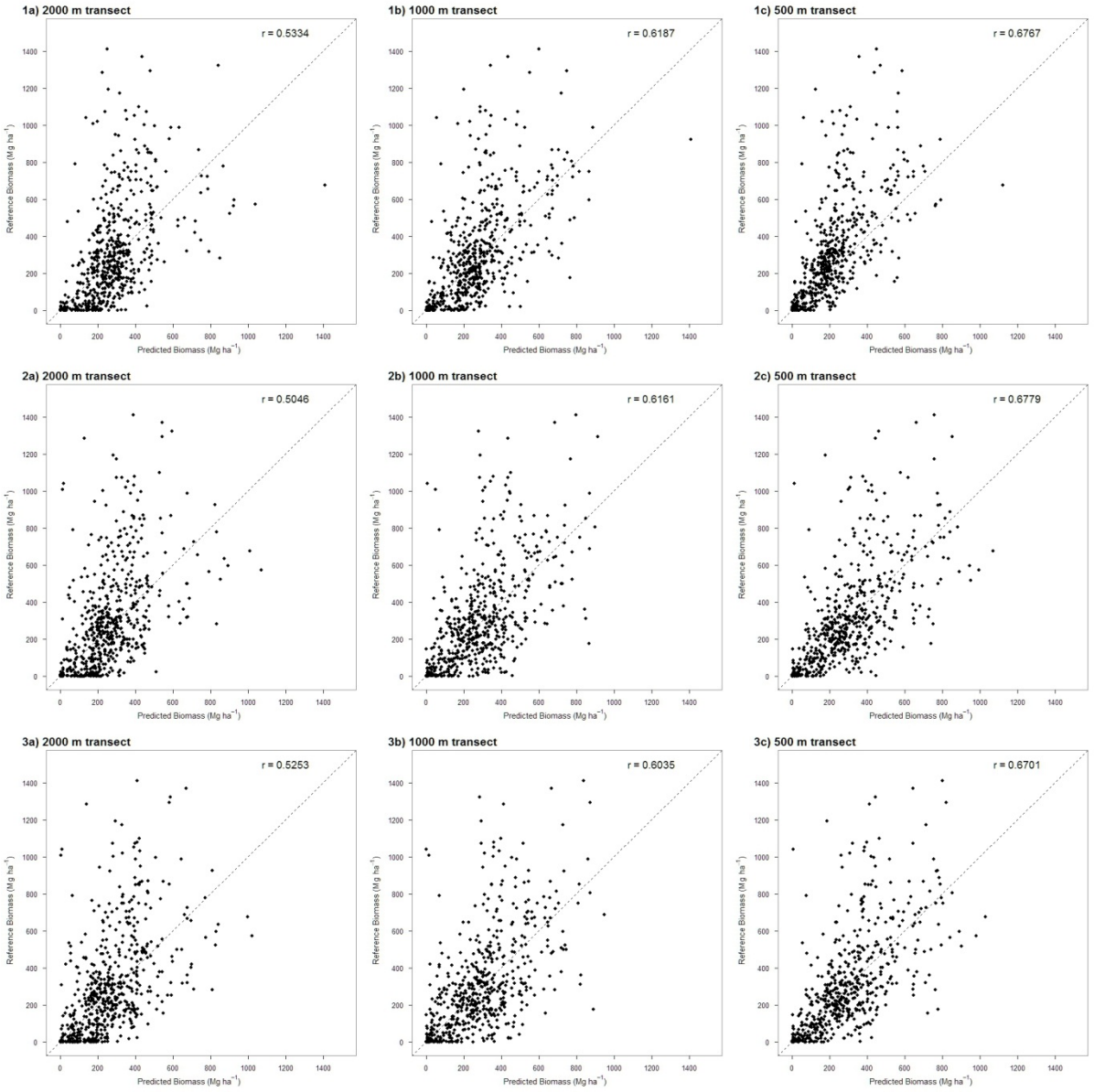

Figure 4.6 Scatterplots of estimated vs. observed aboveground biomass values for all sampling strategies tested. 1. co-kriging (a,b,c); 2. regression kriging (a,b,c); and 3. regression co-kriging (a,b,c). Pearson's correlation coefficient provided for each sampling strategy. Scatterplots represent accuracy of estimated values based on validation points (N = 580).

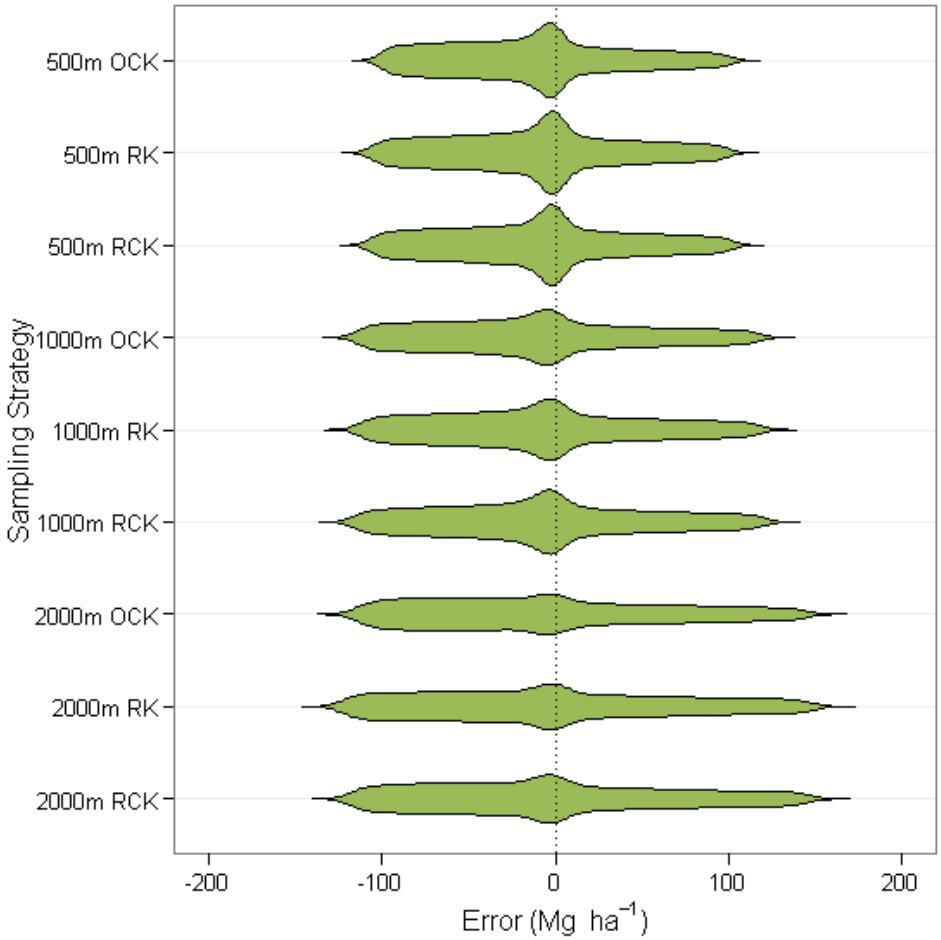

Figure 4.7 Violin plot showing the interquartile range (mid-spread) of residuals in predicted biomass for all sampling strategies tested. OCK - Ordinary Co-kriging; RK – Regression kriging; and RCK – Regression co-kriging.

4.3.2 Biomass mapping models

The kriging-based maps captured the overall variation in aboveground biomass in the study area (Figure 4.1 vs. Figure 4.8). As expected, increase sampling frequency provided better definition of the variation. As a result of the sampling design, artifacts were observed in the co-kriging maps and were more pronounced at the smaller sampling distances. With the regression kriging and regression co-kriging maps, these artifacts were virtually indistinguishable. Biomass maps produced by regression kriging and regression co-kriging were also very similar.

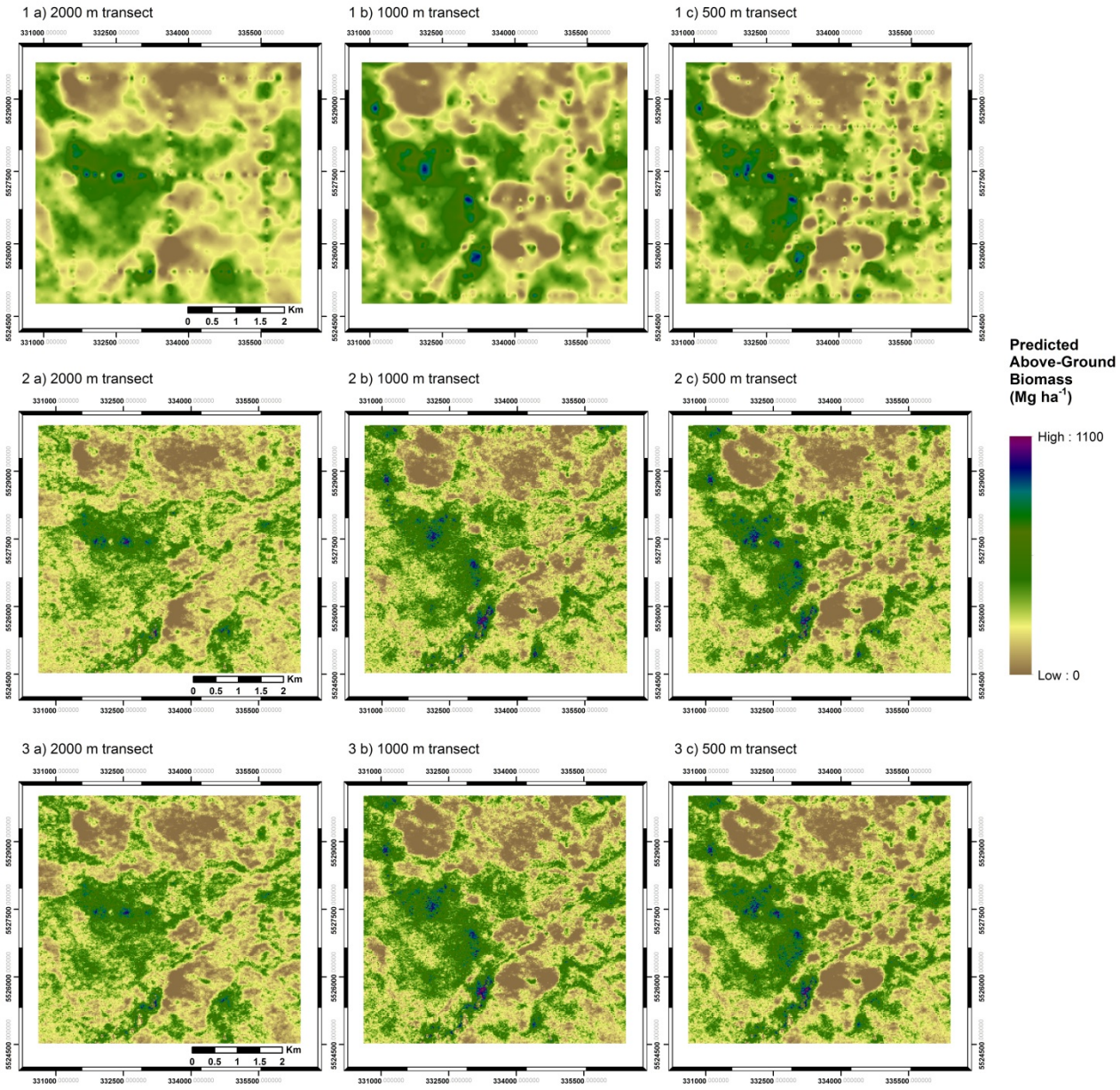

Figure 4.8 Estimated aboveground biomass maps using 1. co-kriging (a,b,c); 2. regression kriging (a,b,c); and 3. regression co-kriging (a,b,c) for all sampling strategies tested.

4.4 Discussion

We found lower errors in predicted biomass with less distance between adjacent sampling transects. Despite some differences observed between kriging methods and sampling strategies, systematic sampling at 1000 m intervals and the use of regression kriging was shown to be a

possible compromise between ease of use, increase in accuracy, and cost of obtaining LiDAR data for this study area. The accuracy of all predictions suffered from low correlation between the LiDAR-derived aboveground biomass estimates and the radar data, which was reflected in the cross-semivariogram by the high nugget and partial sill value. Regardless of the sampling distance between transects, range values at which no spatial dependence was detected was consistently less than 400 m. As a result, the semi-variogram had little influence on the estimation process beyond this distance. This resulted in a smoothing effect, particularly evident when co-kriging was employed. This smoothing effect was less evident in regression kriging and regression co-kriging due to the deterministic portion of these models. Furthermore, the high nugget-effect at a lag distance of zero in the cross-variogram also suggests large variability between the primary and secondary variable. The tendency for kriging to underestimate large values and overestimate small values is supported by previous studies (Hudak et al., 2002; Meng et al., 2009). This tendency may help account for the inflated RMSE values, given that large errors are given disproportional weight because of the squaring of the differences.

Ordinary kriging and co-kriging are the best approaches in cases where spatial interpolation is required, since kriging coefficients rely on the spatial variation between sample points (Hudak et al., 2002). However, for cases of spatial extrapolation however, regression kriging is better suited for spatial extrapolation, since the main kriging coefficients only depend on the correlation between the dependent variable and independent variables (Meng et al., 2009).

4.4.1 Future considerations

The techniques and sampling framework presented in this study are relevant to large area aboveground biomass assessments and identify multi-variable kriging as a robust statistical technique for estimating forest biomass, provided that there is strong correlation between

biomass and the secondary variable. Due to the asymptotic relationships between biomass and radar backscatter, and the high variance between the two, integrating direct radar backscatter and LiDAR using a spatial modeling approach is likely more suited for large area mapping of moderate forest biomass levels where correlation would be expectedly higher. Integrating radar backscatter and LiDAR to estimate areas of high biomass could possibly benefit from aspatial methods as shown by (Tsui et al., 2012). However, such an approach is most suitable for smaller areas where both LiDAR and radar data are available at all locations.

Given that tree heights are known to be highly correlated to biomass, the potential for integrating LiDAR with wall-to-wall canopy heights derived from Polarimetric InSAR (Pol-InSAR) or InSAR is high. By virtue of the properties of radar, InSAR heights usually correspond to the location of the scattering phase center, which typically underestimates actual canopy heights (Balzter et al., 2007). Therefore, although this technique is able to obtain canopy height measurements, integrating them with highly accurate LiDAR observations is one way to obtain high accuracy. The planned suite of future satellites including NASA's Deformation, Ecosystem, Structure, and Dynamics of Ice – Radar (DESDynI-R) L-band mission, Japan's ALOS-2 L-band Mission, and ESA's BIOMASS P-band mission, in addition to the advancements in SAR interferometric processing, such as multiple baseline InSAR (Neumann et al., 2010), and SAR tomography (Reigber and Moreira, 2000), should allow for future operational integration of SAR and LiDAR data. Additionally, new means of optical image understanding and processing are providing novel opportunities for composting that may mitigate the negative impacts of cloud cover (Hansen and Loveland, 2012).

4.4.2 LiDAR sampling framework

Regardless of which secondary variable is selected, highly accurate assessments of forest biomass for large areas will likely require integration with LiDAR observations, whether

airborne or spaceborne. Large area coverage of LiDAR requires a sampling framework, to capture the variation and structural characteristics of the forested area (Wulder et al., 2012b). The cost/benefit of such a sampling framework can be illustrated by performing a basic cost comparison for this study area using the approximate costs in (Wulder et al., 2008). For a total area of 25 km^2, complete airborne LiDAR coverage to obtain a data set with a posting size of 30 cm would cost approximately $1000 CAD per km2 ($25,000 CAD total). Implementing a sampling framework incorporating continuous profiling transects with a swath size of 100 m at the same posting size for every 1000 meters would cost approximately $6,000 CAD, a quarter of the cost of full LiDAR coverage. If accurate tree or stand-level height information is required, LiDAR data may not be considered expensive. However, if lower costs are needed, yet achieving reasonably accurate depiction of stand height or biomass, other data types or modeling approaches may be preferred.

Cost savings generated from a LiDAR sampling framework and a multi-sensor approach would conceivably benefit activities like assessing aboveground carbon stocks and carbon stock change, particularly for tropical areas where forest lands are regularly cloud covered and are inaccessible. Strategies for implementing a LiDAR sampling framework for such a scenario would potentially involve several general steps:

1. Stratify the land primarily into forest land (FL) and non-forest land (NFL) using pre-existing land cover data if available. If such land cover data is not available, separation of broad land cover types can be obtained through the use of SAR as demonstrated by Hoekman et al. (2010) for the island of Borneo. Their study presents a potential method for differentiating land cover types through the use of single-pol and multi-pol L-band SAR data.

2. Acquire space-borne radar at the spatial resolution required to meet information need and use land cover data to mask-out (i.e., remove) areas identified as NFL.
3. Establish a series of sample ground plots for all areas stratified as FL and ensure complete variation in biomass is captured to characterize the population. Then, calculate aboveground biomass through the use of appropriate allometric equations. The number of ground plots will depend on the size of the study area, but also must consider the spatial distribution of individual forest types and also the with-in type variability (Wulder et al., 2012a). A complete discussion is not provided here given the complex nature of sampling design and sampling theory, please refer to Brown (1999).
4. Collect airborne LiDAR data to intersect each of the sample ground plots. Regress calculated aboveground biomass data with the LiDAR measurements to obtain sample aboveground biomass transects. A concise discussion on the use of profiling LiDAR as a sampling tool is provided by Nelson et al. (2003). Because of the nature of how airborne LiDAR data is collected (i.e., linear flight lines) Wulder et al. (2012a) suggests possible sampling designs that can be used.
5. Estimate and model the semi-variogram from the LiDAR transects and in combination with SAR data and predict aboveground biomass for un-sampled locations using regression kriging.
6. Finally, complete quantitative validation to compare predicted values to actual values. Reference data may consist of new ground plot data or an independent subset of LiDAR transects not used in the modeling processing.

.

5. CONCLUSION

The removal of terrestrial carbon through the conversion of forested to non-forested land will continue to have important impacts on GHG concentrations in the atmosphere. To support the reporting requirements of global climate change agreements and aid climate mitigation programmes, such as REDD+, use of Earth observation satellite data are increasingly crucial given that most developing countries have large areas of forest that are difficult to access and systematically monitor (Grainger and Obersteiner, 2011). There is notable capacity for LiDAR and SAR technologies to provide objective, practical, and cost-effective solutions to monitor changes in forest area and estimate aboveground carbon stocks. The IPCC Good Practice Guidelines for National Greenhouse Gas Inventories for Agriculture, Forestry, and Other Land Use (IPCC 2006) and Global Observation of Forest and Land Cover Dynamics (GOFC-GOLD) Sourcebook (GOFC-GOLD 2011) recommend the use of both LiDAR and SAR to support carbon stock assessment among other data sources such as multi-spectral data or targeted airborne surveys.

The overall objective of this thesis was to demonstrate novel methods to integrate two remotely sensed data sets (i.e., SAR and LiDAR) for the application of forest biomass estimation. This research was divided into two main questions: (1) can shorter wavelength radar variables provide improved biomass estimates when combined aspatially with LiDAR data; and (2) can the use of space-borne radar extend aboveground biomass estimates over a larger area using spatial modeling methods. In addition to these two main questions, insights into the various relationships between biomass and SAR polarimetry and coherence were gained, while a new approach was investigated to predict forest biomass from LiDAR data across the landscape.

5.1 Key Findings

Results from chapter 3 suggest that integrating radar variables into a LiDAR-derived model of forest biomass can provide added explanatory information to biomass estimates, with improvements in relative RMSE of approximately 10%. It also showed that repeat-pass InSAR coherence magnitudes, from a combination of C-band and L-band radar, provides the best estimate of forest biomass and are the most significantly correlated radar variables. Similar observations were also made by Delbart et al. (2002) for L-band data. In contrast, backscatter, polarimetric decomposition, and interferometric coherence do not have good correlations (i.e., 0.36 and 040 respectively) to with biomass components. As reported by Melon et al. (2002), a higher dynamic range is provided by backscatter than polarimetic measurements when assessing forest biomass. Including C-band radar data in a LiDAR-derived biomass model also indicated that additional information in crown biomass was obtainable.

Cost implications are important factors to consider before applying these results. At current data costs, obtaining both LiDAR and radar data for moderate improvements in the accuracy of biomass estimates is not practical. However, movement towards open data policies for Earth observation data (Aschbacher and Milagro-Pérez, 2012) provide an exciting possibility for future use of radar and multi-spectral sensors. This movement towards open exchange of remote sensing data also promotes efficient data dissemination and advances in data delivery technologies. Also open data policies advance data processing levels to provide well calibrated products to allow for wider public usage. The Sentinel-1 satellite, the first of a two radar satellites planned to be launched in mid-2013, carries on the legacy of European C-band radar sensors including the European Remote Sensing satellites (ERS-1/2) and Envisat Advanced SAR. With planned repeat cycles of less than 14-days and average revisits of 2-days once both satellite are operational (Torres et al., 2012), Sentinel-1 data can aid in global monitoring of forested land at high spatial resolution (Malenovský et al., 2012). Furthermore, NASA's

proposed Deformation, Ecosystem Structure and Dynamics of Ice (DESDynI-R) satellite will have a L-band SAR system with a potential repeat cycle of 8 to 12-days and will offer large area observations (Eisen et al., 2012). Current agreements for open data access for Sentinel-1 and ongoing discussions for DESDynI–R and the next generation Advanced Land Observing Satellite (ALOS-2), integrating LiDAR and SAR data at collocated sites has greater potential.

Results from chapter 4 focused on the accuracy of three kriging techniques for estimating aboveground biomass at a spatial resolution of 30 m. The study demonstrated how samples of forest biomass, derived from airborne LiDAR and plot data, can be combined with wall-to-wall spaceborne radar observations to achieve spatially continuous biomass estimates. In this integrative framework, spatial modeling methods provide an effective means to overcome challenges in the application of large area biomass assessments. Through additional research on the sampling design and on landscape stratification, accuracy of biomass estimates can potentially be improved. Integration of LiDAR and space-borne radar data offer a different approach for direct assessments of biomass, especially where comprehensive forest inventory data do not exist or are too expensive to obtain, and where frequent cloud cover make other methods of quantifying forest biomass challenging. The wall-to-wall mapping opportunity enabled through integrating LiDAR and radar data provides additional value to existing data augmenting plot-based biomass estimates (De Sy et al., 2012). Accurate biomass maps are possible, provided appropriate samples of LiDAR-based biomass area available and these samples represent the population statistically and geographically. Potential next steps would be to compare this approach to the more common “combine and assign” or “stratify and multiply” methods (Goetz et al., 2009) and examine the errors associated with each. Ultimately, any remote sensing-based monitoring system must be able to measure changes in forest area at a fine spatial scale (e.g. ~ 1 ha) and carbon stock consistently over the longer term to be able to support a REDD+ MRV system (DeFries et al., 2007; GOFC-GOLD, 2011).

5.2 Limitations of Study

This thesis presented two potential methods for integrating LiDAR and radar data. Several limitations and caveats for each study are described below:

Sample Size: The number of field plots used in the study presented in chapter 3 was small. Given the small sample size, all samples were used for model fitting. The robustness of the observed relationship and extrapolation of the results should be interpreted cautiously. Independent plots for validation could not be established and measured due to harvesting of the study site in 2011.

Misalignment of dates: The data sources used in chapter3 and 4 were not temporally coherent (i.e., they were acquired on different dates). Although discussed and addressed in section 3.2.2, the acquisition of data from different dates does introduce uncertainties in the estimates. No assessment of this uncertainty was possible given no LiDAR and PALSAR data was available for 2010.

Co-variance of LiDAR and SAR data: The accuracy of forest biomass estimates suffered from low correlation between the LiDAR-derived aboveground biomass estimates and the radar data, as discussed in Section 4.4. This in turn affected the distance where spatial dependency was observed in the kriging process. The full potential of radar data (i.e. InSAR heights) could not be investigated given that appropriate data, such as single-pass InSAR data, were not available.

Forest type: Integration approaches investigated in this thesis were applied to a coastal temperate forest which had high levels of biomass. The portability of these approaches to the boreal forest or tropical forest biomes was not investigated. The higher correlation between radar measurements and low to moderate biomass levels suggests that the accuracy in biomass estimates may be better in boreal forests. In contrast, dense tropical forests with a substantially

dense understory may limit the information content from C-band radar since the microwave pulse would be mainly attenuated within the upper canopy.

Biomass monitoring: Although determining baseline carbon stocks is necessary, under the UNFCCC REDD+, monitoring and assessing forest carbon stock changes is required to measure emissions across time. The results from chapter 4 provided carbon stock amounts for only one time period. No investigation was made on the monitoring capability of the proposed approach. However, the monitoring capacity of LiDAR reported by Bater et al. (2011) does suggest potential.

5.3 Future Research

This research has highlighted the importance of exploiting the synergies between multiple sensors. However, potential key synergies between multiple sensors are mainly the subject of research and are not operationally applied (De Sy et al., 2012). Acknowledging the limitations of this research, a number of areas on which future research could focus on are:

- Determining if C-band radar entropy and InSAR coherence provide similar relationships when the sample population size is increased;

- Investigating the use of kriging with InSAR derived heights, to exploit the stronger correlation between the LiDAR and radar-derived heights and thereby provide improved accuracy in biomass estimates. However, due to the uncertainty of obtaining raw interferometric TamDEM-X data, this investigation may be limited to airborne InSAR data collection campaigns or future space-borne radar sensors;

- Assessing the portability of these methods to other forest biomes, such as tropical or boreal forests. With the boreal forest covering approximately 77% of Canada's forested land (Wulder et al., 2007) and providing an important carbon sink (Apps et al., 1995),

investigating other potential methods to assess this large forest area can be important in understanding forest carbon stocks in northern Canada; and

- Determining if spatial modeling techniques are viable methods for monitoring and assessing changes in carbon stocks. Although LiDAR data collected from different passes can provide similar vertical characteristics (Bater et al., 2011), determining whether spatial kriging can measure carbon stocks over time is not known.

Understanding the complementary ways in which accurate LiDAR data can be integrated with space-borne radar to characterize forests is an active area of research. In this thesis, I examined two areas of study related to data integration for biomass estimation. With advancements offered by future sensors (e.g., higher revisit times, higher spatial resolutions, etc.), advances in image processing (i.e., image composting to reduce the impact of cloud cover), and advances in policies (i.e., open data access), studies into multi-sensor synergies for forest biomass assessments will continue. Results from these studies add to the growing body of knowledge examining carbon stock assessments using remotely sensed data.

REFERENCES

Ahrends, A., Burgess, N.D., Milledge, S.A.H., Bulling, M.T., Fisher, B., Smart, J.C.R., Clarke, G.P., Mhoro, B.E., Lewis, S.L., 2010. Predictable waves of sequential forest degradation and biodiversity loss spreading from an African city. Proceedings of the National Academy of Sciences 107, 14556–14561.

Akaike, H., 1973. Information theory and an extension of the maximum likelihood principle, in: Second International Symposium on Information Theory. pp. 267–281.

Alsamamra, H., Ruiz-Arias, J.A., Pozo-Vázquez, D., Tovar-Pescador, J., 2009. A comparative study of ordinary and residual kriging techniques for mapping global solar radiation over southern Spain. Agricultural and Forest Meteorology 149, 1343–1357.

Apps, M.J., Price, D.T., Wisniewski, 1995. Boreal forests and global change. Kluwer Academic Publishers, Boston, MA (United States).

Aschbacher, J., Milagro-Pérez, M.P., 2012. The European Earth monitoring (GMES) programme: Status and perspectives. Remote Sensing of Environment 120, 3–8.

Asner, G.P., Powell, G.V.N., Mascaro, J., Knapp, D.E., Clark, J.K., Jacobson, J., Kennedy-Bowdoin, T., Balaji, A., Paez-Acosta, G., Victoria, E., Secada, L., Valqui, M., Hughes, R.F., 2010. High-resolution forest carbon stocks and emissions in the Amazon. PNAS 107, 16738–16742.

Balzter, H., Luckman, A., Skinner, L., Rowland, C., Dawson, T., 2007. Observations of forest stand top height and mean height from interferometric SAR and LiDAR over a conifer plantation at Thetford Forest, UK. International Journal of Remote Sensing 28, 1173–1197.

Bater, C.W., Wulder, M.A., Coops, N.C., Nelson, R.F., Hilker, T., Nasset, E., 2011. Stability of Sample-Based Scanning-LiDAR-Derived Vegetation Metrics for Forest Monitoring. IEEE Transactions on Geoscience and Remote Sensing 49, 2385 –2392.

Bellard, C., Bertelsmeier, C., Leadley, P., Thuiller, W., Courchamp, F., 2012. Impacts of climate change on the future of biodiversity. Ecology Letters 15, 365–377.

Bivand, R.S., Pebesma, E.J., Gómez-Rubio, V., 2008. Applied spatial data analysis with R. Springer, New York.

British Columbia. 2011. Protocol for the Creation of Forest Carbon Offsets in British Columbia, http://www.env.gov.bc.ca/cas/mitigation/ggrta/pdf/offsets-reg.pdf (Accessed 22 January, 2013)

British Columbia. 2008. Greenhouse Gas Reduction Targets Act: Emission Offsets Regulation, http://www.env.gov.bc.ca/cas/mitigation/pdfs/Forest_Carbon_Offset_Protocol_v1_0_Web.pdf (Accessed 22 January, 2013)

Brown, S., 1999. Guidelines for inventorying and monitoring carbon offsets in forest-based projects. Winrock International, Arlington, VA.

Brown, S. (1997). Estimating biomass and biomass change of tropical forests: a primer (Vol. 134). Food & Agriculture Org..

Campbell, B.M., 2009. Beyond Copenhagen: REDD+, agriculture, adaptation strategies and poverty. Global Environmental Change 19, 397–399.

Canadell, J.G., Quéré, C.L., Raupach, M.R., Field, C.B., Buitenhuis, E.T., Ciais, P., Conway, T.J., Gillett, N.P., Houghton, R.A., Marland, G., 2007. Contributions to accelerating atmospheric CO2 growth from economic activity, carbon intensity, and efficiency of natural sinks. PNAS 104, 18866–18870.

Castel, T., Beaudoin, A., Stach, N., Stussi, N., Toan, T.L., Durand, P., 2001. Sensitivity of space-borne SAR data to forest parameters over sloping terrain. Theory and experiment. International Journal of Remote Sensing 22, 2351–2376.

Chapin, F.S., McGuire, A.D., Ruess, R.W., Hollingsworth, T.N., Mack, M.C., Johnstone, J.F., Kasischke, E.S., Euskirchen, E.S., Jones, J.B., Jorgenson, M.T., Kielland, K., Kofinas, G.P., Turetsky, M.R., Yarie, J., Lloyd, A.H., Taylor, D.L., 2010. Resilience of Alaska's boreal forest to climatic change. Canadian Journal of Forest Research 40, 1360–1370.

Cloude, S.R., Papathanassiou, K.P., 1998. Polarimetric SAR interferometry. IEEE Transactions on Geoscience and Remote Sensing 36, 1551–1565.

Cloude, S.R., Pottier, E., 1997. An entropy based classification scheme for land applications of polarimetric SAR. IEEE Transactions on Geoscience and Remote Sensing 35, 68–78.

Coops, N.C., Hilker, T., Wulder, M.A., St-Onge, B., Newnham, G., Siggins, A., Trofymow, J.A.., 2007. Estimating canopy structure of Douglas-fir forest stands from discrete-return LiDAR. Trees Structure and Function 21, 295–310.

Coops, N.C., Waring, R.H., 2011. Estimating the vulnerability of fifteen tree species under changing climate in Northwest North America. Ecological Modelling 222, 2119–2129.

Corbera, E., Soberanis, C.G., Brown, K., 2009. Institutional dimensions of Payments for Ecosystem Services: An analysis of Mexico's carbon forestry programme. Ecological Economics 68, 743–761.

Curran, P.J., 1988. The semivariogram in remote sensing: An introduction. Remote Sensing of Environment 24, 493–507.

Curran, P.J., Atkinson, P.M., 1998. Geostatistics and remote sensing. Progress in Physical Geography 22, 61 –78.

De Sy, V., Herold, M., Achard, F., Asner, G.P., Held, A., Kellndorfer, J., Verbesselt, J., 2012. Synergies of multiple remote sensing data sources for REDD+ monitoring. Current Opinion in Environmental Sustainability 4, 696–706.

DeFries, R., Achard, F., Brown, S., Herold, M., Murdiyarso, D., Schlamadinger, B., De Souza Jr., C., 2007. Earth observations for estimating greenhouse gas emissions from deforestation in developing countries. Environmental Science & Policy 10, 385–394.

Delbart, N., Melon, P., Florsch, G., Le Toan, T., Martinez, J.-M., 2002. Forest biomass retrieval using L-band polarimetric measurements, in: IEEE Geoscience and Remote Sensing Symposium, 2002. IGARSS '02. Presented at the Geoscience and Remote Sensing Symposium, 2002. IGARSS '02. 2002 IEEE International, pp. 1789 – 1791 vol.3.

Dixon, R.K., Brown, S., Houghton, R.A., Solomon, A.M., Trexler, M.C., Wisniewski, J., 1994. Carbon pools and flux of global forest ecosystems. Science 263, 185–189.

Dobson, M.C., Ulaby, F.T., LeToan, T., Beaudoin, A., Kasischke, E.S., Christensen, N., 1992. Dependence of radar backscatter on coniferous forest biomass. IEEE Transactions on Geoscience and Remote Sensing 30, 412–415.

Duncanson, L., Niemann, K., Wulder, M., 2010. Integration of GLAS and Landsat TM data for aboveground biomass estimation. Canadian Journal of Remote Sensing 36, 129–141.

Eisen, H.J., Jai, B., Rosen, P.A., Veilleux, L., Xaypraseuth, P., 2012. Conceptual development of the DESDynI mission, in: 2012 IEEE Aerospace Conference. Presented at the 2012 IEEE Aerospace Conference, pp. 1 –10.

Franklin, S.E., Lavigne, M.B., Wulder, M.A., Stenhouse, G.B., 2002. Change detection and landscape structure mapping using remote sensing. The Forestry Chronicle 78, 618–625.

Gaveau, D.L.., Balzter, H., Plummer, S., 2003. Forest woody biomass classification with satellite-based radar coherence over 900 000 km2 in Central Siberia. Forest Ecology and Management 174, 65–75.

Gibbs, H.K., Brown, S., Niles, J.O., Foley, J.A., 2007. Monitoring and estimating tropical forest carbon stocks: making REDD a reality. Environmental Research Letters 2, 1–13.

Gillis, M.D., Leckie, D.G., 1993. Forest inventory mapping procedures across Canada. Information Report PI-X-122. Petawawa: Natural Resources Canada, Information Report PI-X-122. Petawawa: Natural Resources Canada.

Goetz, S.J., Baccini, A., Laporte, N.T., Johns, T., Walker, W., Kellndorfer, J., Houghton, R.A., Sun, M., 2009. Mapping and monitoring carbon stocks with satellite observations: a comparison of methods. Carbon Balance and Management 4, 2.

GOFC-GOLD, 2010. A sourcebook of methods and procedures for monitoring and reporting nthropogenic greenhouse gas emissions and removals caused by deforestation, gains and losses of carbon stocks in forests remaining forests, and forestation. GOFC-GOLD Project Office, hosted by Natural Resources Canada, Alberta, Canada.

Goodwin, G., 1937. Regeneration study on the logged-off lands of the Comox Logging and Railway Company Oyster River forest survey. B. C. Forest Service, Canada.

Goovaerts, P., 1997. Geostatistics for natural resources evaluation. Oxford University Press, New York.

Grainger, A., Obersteiner, M., 2011. A framework for structuring the global forest monitoring landscape in the REDD+ era. Environmental Science & Policy 14, 127–139.

Greig, M., Bull, G., 2011. Carbon Management in British Columbia's Forests: An Update on Opportunities and Challenges. Journal of Ecosystems and Management 12.

Hall, S.A., Burke, I.C., Box, D.O., Kaufmann, M.R., Stoker, J.M., 2005. Estimating stand structure using discrete-return lidar: an example from low density, fire prone ponderosa pine forests. Forest Ecology and Management 208, 189–209.

Hansen, M.C., Loveland, T.R., 2012. A review of large area monitoring of land cover change using Landsat data. Remote Sensing of Environment 122, 66–74.

Harshaw, H.W., Sheppard, S.R.J., Jeakins, P., 2009. Public attitudes toward sustainable forest management: Opinions from forest-dependent communities in British Columbia. About the cover photograph: Regeneration on the right of the watercourse reflects 81.

Hilker, T., Van Leeuwen, M., Coops, N.C., Wulder, M.A., Newnham, G.J., Jupp, D.L.., Culvenor, D.S., 2010. Comparing canopy metrics derived from terrestrial and airborne laser scanning in a Douglas-fir dominated forest stand. Trees Structure and Function 24, 1–14.

Hoekman, D.H., Vissers, M.A.M., Wielaard, N., 2010. PALSAR wide-area mapping of Borneo: Methodology and map validation. IEEE Journal of Selected Topics in Applied Earth Observations and Remote Sensing 3, 605–617.

Hudak, A.T., Lefsky, M.A., Cohen, W.B., Berterretche, M., 2002. Integration of lidar and Landsat ETM+ data for estimating and mapping forest canopy height. Remote Sensing of Environment 82, 397–416.

Hyde, P., Dubayah, R., Walker, W., Blair, J.B., Hofton, M., Hunsaker, C., 2006. Mapping forest structure for wildlife habitat analysis using multi-sensor (LiDAR, SAR/InSAR, ETM+, Quickbird) synergy. Remote Sensing of Environment 102, 63–73.

Hyde, P., Nelson, R., Kimes, D., Levine, E., 2007. Exploring LiDAR-RaDAR synergy - predicting aboveground biomass in a southwestern ponderosa pine forest using LiDAR, SAR and InSAR. Remote Sensing of Environment 106, 28–38.

Imhoff, M.L., 1995a. Radar backscatter and biomass saturation: ramifications for global biomass inventory. IEEE Transactions on Geoscience and Remote Sensing 33, 511–518.

Imhoff, M.L., 1995b. A theoretical analysis of the effect of forest structure on synthetic aperture radar backscatter and the remote sensing of biomass. IEEE Transactions on Geoscience and Remote Sensing 33, 341–352.

IPCC, 2006. Guidelines for National Greenhouse Gas Inventories. Vol. 4. Agriculture, forestry and other land use. Chapter 4 - Forest Land (available at http://www.ipcc-nggip.iges.or.jp/public/2006gl/pdf/4_Volume4/V4_04_Ch4_Forest_Land.pdf).

IPCC, 2007. Climate change 2007: synthesis report (AR7). Intergovernmental Panel on Climate Change, Geneva.

Johnson, W.C., Sharpe, D.M., 1983. The ratio of total to merchantable forest biomass and its application to the global carbon budget. Canadian Journal of Forest Research 13, 372–383.

Journel, A.G., Huijbregts, C.J., 1978. Mining geostatistics. Academic Press, London.

Kangas, A., Grove, J.H., Scott, C.T., 2006. Forest inventory: methodology and applications. Spinger, Netherlands.

Kasischke, E.S., Melack, J.M., Craig Dobson, M., 1997. The use of imaging radars for ecological applications–A review. Remote Sensing of Environment 59, 141–156.

Kasischke, E.S., Tanase, M.A., Bourgeau-Chavez, L.L., Borr, M., 2011. Soil moisture limitations on monitoring boreal forest regrowth using spaceborne L-band SAR data. Remote Sensing of Environment 115, 227–232.

Kellndorfer, J.M., Pierce, L.E., Dobson, M.C., Ulaby, F.T., 1998. Toward consistent regional-to-global-scale vegetation characterization using orbital SAR systems. IEEE Transactions on Geoscience and Remote Sensing 36, 1396–1411.

Kimberly, C.M., Curran, L.M., 2009. REDD pilot project scenarios: are costs and benefits altered by spatial scale? Environmental Research Letters 4, 031003.

Koch, B., 2010. Status and future of laser scanning, synthetic aperture radar and hyperspectral remote sensing data for forest biomass assessment. ISPRS Journal of Photogrammetry and Remote Sensing 65, 581–590.

Kraus, K., Pfeifer, N., 1998. Determination of terrain models in wooded areas with airborne laser scanner data. ISPRS Journal of Photogrammetry and Remote Sensing 53, 193–203.

Krige, D.G., 1966. Two-dimensional weighted moving average trend surfaces for ore-evaluation. Journal of the South African Institute of Mining and Metallurgy 66, 13–38.

Kurz, W.A., Apps, M.J., 2006. Developing Canada's National Forest Carbon Monitoring, Accounting and Reporting System to Meet the Reporting Requirements of the Kyoto Protocol. Mitigation and Adaptation Strategies for Global Change 11, 33–43.

Kurz, W.A., Dymond, C.C., White, T.M., Stinson, G., Shaw, C.H., Rampley, G.J., Smyth, C., Simpson, B.N., Neilson, E.T., Trofymow, J.A., Metsaranta, J., Apps, M.J., 2009. CBM-CFS3: A model of carbon-dynamics in forestry and land-use change implementing IPCC standards. Ecological Modelling 220, 480–504.

Lambert, M.C., Ung, C.H., Raulier, F., 2005. Canadian national tree aboveground biomass equations. Canadian Journal of Forest Research 35, 1996–2018.

Le Toan, T., Beaudoin, A., Riom, J., Guyon, D., 1992. Relating forest biomass to SAR data. IEEE Transactions on Geoscience and Remote Sensing 30, 403–411.

Leaps, 2009. Regression subset selection – Package 'leaps', http://cran.r-project.org/web/packages/leaps/leaps.pdf (Accessed 15 July, 2012)

Lefsky, M.A., Cohen, W.B., Acker, S.A., Parker, G.G., Spies, T.A., Harding, D., 1999. Lidar Remote Sensing of the Canopy Structure and Biophysical Properties of Douglas-Fir Western Hemlock Forests. Remote Sensing of Environment 70, 339–361.

Lefsky, M.A., Cohen, W.B., Harding, D.J., Parker, G.G., Acker, S.A., Gower, S.T., 2002. Lidar remote sensing of above-ground biomass in three biomes. Global Ecology and Biogeography 11, 393–399.

Lewis, S.L., Lopez-Gonzalez, G., Sonké, B., Affum-Baffoe, K., Baker, T.R., Ojo, L.O., Phillips, O.L., Reitsma, J.M., White, L., Comiskey, J.A., Djuikouo K., M.-N., Ewango, C.E.N., Feldpausch, T.R., Hamilton, A.C., Gloor, M., Hart, T., Hladik, A., Lloyd, J., Lovett, J.C., Makana, J.-R., Malhi, Y., Mbago, F.M., Ndangalasi, H.J., Peacock, J., Peh, K.S.-H., Sheil, D., Sunderland, T., Swaine, M.D., Taplin, J., Taylor, D., Thomas, S.C., Votere, R., Wöll, H., 2009. Increasing carbon storage in intact African tropical forests. Nature 457, 1003–1006.

Li, Y., Andersen, H.E., McGaughey, R., 2008. A comparison of statistical methods for estimating forest biomass from light detection and ranging data. Western Journal of Applied Forestry 23, 223–231.

Lim, K.S., Treitz, P.M., 2004. Estimation of above ground forest biomass from airborne discrete return laser scanner data using canopy-based quantile estimators. Scandinavian Journal of Forest Research 19, 558–570.

Lucas, R.M., Cronin, N., Lee, A., Moghaddam, M., Witte, C., Tickle, P., 2006. Empirical relationships between AIRSAR backscatter and LiDAR-derived forest biomass, Queensland, Australia. Remote Sensing of Environment 100, 407–425.

Lutz, D.A., Washington-Allen, R.A., Shugart, H.H., 2008. Remote sensing of boreal forest biophysical and inventory parameters: a review. Canadian Journal of Remote Sensing 34, 286–313.

Malenovský, Z., Rott, H., Cihlar, J., Schaepman, M.E., García-Santos, G., Fernandes, R., Berger, M., 2012. Sentinels for science: Potential of Sentinel-1, -2, and -3 missions for scientific observations of ocean, cryosphere, and land. Remote Sensing of Environment 120, 91–101.

Matheron, G., 1971. The Theory of Regionalizaed Variables and Its Applications. Cahiers Centre de Morphologie Mathematique, Fontaineblue.

McGaughey, R.J., 2009. FUSION/LDV: software for LIDAR data analysis and visualization. US Department of Agriculture, Forest Service, Pacific Northwest Research Station: Seattle, WA, USA 123.

Meidinger, D.V., Pojar, J., 1991. Ecosystems of British Columbia. Research Branch, Ministry of Forests, Victoria.

Melon, P., Le Toan, T., Picard, G., Delbart, N., Davidson, M., 2002. On the information content of L-band polarimetric SAR data over forested areas.

Meng, Q., Cieszewski, C., Madden, M., 2009. Large area forest inventory using Landsat ETM+: A geostatistical approach. ISPRS Journal of Photogrammetry and Remote Sensing 64, 27–36.

Metsaranta, J.M., Dymond, C.C., Kurz, W.A., Spittlehouse, D.L., 2011. Uncertainty of 21st century growing stocks and GHG balance of forests in British Columbia, Canada resulting from

potential climate change impacts on ecosystem processes. Forest Ecology and Management 262, 827–837.

Miles, L., Kapos, V., 2008. Reducing Greenhouse Gas Emissions from Deforestation and Forest Degradation: Global Land-Use Implications. Science 320, 1454–1455.

Mitchard, E.T.A., Saatchi, S.S., White, L.J.T., Abernethy, K.A., Jeffery, K.J., Lewis, S.L., Collins, M., Lefsky, M.A., Leal, M.E., Woodhouse, I.H., Meir, P., 2012. Mapping tropical forest biomass with radar and spaceborne LiDAR in Lopé National Park, Gabon: overcoming problems of high biomass and persistent cloud. Biogeosciences 9, 179–191.

Moghaddam, M., Dungan, J.L., Acker, S., 2002. Forest variable estimation from fusion of SAR and multispectral optical data. IEEE Transactions on Geoscience and Remote Sensing 40, 2176– 2187.

Morgenstern, K., Black, A.T., Humphreys, E.R., Griffis, T.J., Drewitt, G.B., Cai, T., Nesic, Z., Spittlehouse, D.L., Livingston, N.J., 2004. Sensitivity and uncertainty of the carbon balance of a Pacific Northwest Douglas-fir forest during an El Niño/La Niña cycle. Agricultural and Forest Meteorology 123, 201–219.

Murphy, A.H., Katz, R.W., 1985. Probability, statistics, and decision making in the atmospheric sciences. Westview Press, Boulder, Colorado.

Næsset, E., 1997. Determination of mean tree height of forest stands using airborne laser scanner data. ISPRS Journal of Photogrammetry and Remote Sensing 52, 49–56.

Næsset, E., 2002. Predicting forest stand characteristics with airborne scanning laser using a practical two-stage procedure and field data. Remote Sensing of Environment 80, 88–99.

Næsset, E., Bollandsås, O.M., Gobakken, T., 2005. Comparing regression methods in estimation of biophysical properties of forest stands from two different inventories using laser scanner data. Remote Sensing of Environment 94, 541–553.

Næsset, E., Gobakken, T., 2005. Estimating forest growth using canopy metrics derived from airborne laser scanner data. Remote Sensing of Environment 96, 453–465.

Næsset, E., Gobakken, T., 2008. Estimation of above- and below-ground biomass across regions of the boreal forest zone using airborne laser. Remote Sensing of Environment 112, 3079–3090.

Næsset, E., Gobakken, T., Solberg, S., Gregoire, T.G., Nelson, R., Ståhl, G., Weydahl, D., 2011. Model-assisted regional forest biomass estimation using LiDAR and InSAR as auxiliary data: A case study from a boreal forest area. Remote Sensing of Environment 115, 3599–3614.

Næsset, E., Økland, T., 2002. Estimating tree height and tree crown properties using airborne scanning laser in a boreal nature reserve. Remote Sensing of Environment 79, 105–115.

Nelson, R., Valenti, M.A., Short, A., Keller, C., 2003. A multiple resource inventory of Delaware using airborne laser data. BioScience 53, 981–992.

Nelson, R.F., Hyde, P., Johnson, P., Emessiene, B., Imhoff, M.L., Campbell, R., Edwards, W., 2007. Investigating RaDAR-LiDAR synergy in a North Carolina pine forest. Remote Sensing of Environment 110, 98–108.

Neumann, M., Ferro-Famil, L., Reigber, A., 2010. Estimation of forest structure, ground, and canopy layer characteristics from multibaseline polarimetric interferometric SAR data. IEEE Transactions on Geoscience and Remote Sensing 48, 1086 –1104.

Olea, R.A., 1977. Measuring spatial dependence with semivariograms. Kansas Geological Survey, Lawrence, Kansas.

Oreskes, N., 2004. The Scientific Consensus on Climate Change. Science 306, 1686.

Pan, Y., Birdsey, R.A., Fang, J., Houghton, R., Kauppi, P.E., Kurz, W.A., Phillips, O.L., Shvidenko, A., Lewis, S.L., Canadell, J.G., Ciais, P., Jackson, R.B., Pacala, S.W., McGuire, A.D., Piao, S., Rautiainen, A., Sitch, S., Hayes, D., 2011. A Large and Persistent Carbon Sink in the World's Forests. Science 333, 988–993.

Parmesan, C., Yohe, G., 2003. A globally coherent fingerprint of climate change impacts across natural systems. Nature 421, 37–42.

Pebesma, E.J., 2004. Multivariable geostatistics in S: the gstat package. Computers & Geosciences 30, 683–691.

Penman, J., Gytarsky, M., Hiraishi, T., Krug, T., Kruger, D., Pipatti, R., Buendia, L., Miwa, K., Ngara, T., Tanabe, K., others, 2003. IPCC good practice guidance for land use, land-use change and forestry. Institute for Global Environmental Strategies.

Peters, G.P., Andrew, R.M., Boden, T., Canadell, J.G., Ciais, P., Quéré, C.L., Marland, G., Raupach, M.R., Wilson, C., 2013. The challenge to keep global warming below 2 °C. Nature Climate Change 3, 4–6.

Pistorius, T., 2012. From RED to REDD+: the evolution of a forest-based mitigation approach for developing countries. Current Opinion in Environmental Sustainability 1 – 8.

Prentice, I.C., Farquhar, G.D., Fasham, M.J.R., Goulden, M.L., Heimann, M., et al., 2001. The carbon cycle and atmospheric carbon dioxide, in: Climate change 2001: the scientific basis: contribution of Working Group I to the Third Assessment Report of the Intergouvernmental Panel on Climate Change. Cambridge University Press, Cambridge, pp. 183–237.

Ranson, K.J., Sun, G., 1997. An evaluation of AIRSAR and SIR-C/X-SAR images for mapping northern forest attributes in Maine, USA. Remote Sensing of Environment 59, 203–222.

Reichle, D.E., Dinger, B.E., Edwards, N.T., Harris, W.F., and Sollins, P., 1973. Carbon flow and storage in a woodland ecosystem. In Carbon and the biosphere. Edited by G.M. Woodwell and E.V. Pecan. AEC Symp. Ser. No. 30. Tech IN

Reigber, A., Moreira, A., 2000. First demonstration of airborne SAR tomography using multibaseline L-band data. IEEE Transactions on Geoscience and Remote Sensing 38, 2142 –2152.

Rignot, E., Way, J., Williams, C., Viereck, L., 1994. Radar estimates of aboveground biomass in boreal forests of interior Alaska. IEEE Transactions on Geoscience and Remote Sensing 32, 1117–1124.

Ristea, C., Maness, T.C., 2009. Opportunities, challenges and markets for forest carbon offset projects. The Forestry Chronicle 85, 715–718.

Romijn, E., Herold, M., Kooistra, L., Murdiyarso, D., Verchot, L., 2012. Assessing capacities of non-Annex I countries for national forest monitoring in the context of REDD+. Environmental Science & Policy 19–20, 33–48.

Rosen, P.A., Hensley, S., Joughin, I.R., Li, F.K., Madsen, S.N., Rodriguez, E., Goldstein, R.M., 2000. Synthetic aperture radar interferometry. Proceedings of the IEEE 88, 333–382.

Rosenqvist, A., Shimada, M., Watanabe, M., Tadono, T., Yamauchi, K., 2004. Implementation of systematic data observation strategies for ALOS PALSAR, PRISM and AVNIR-2, in: Proc. IEEE International Geoscience and Remote Sensing Symposium, 2004. pp. 4527–4530.

Roy, D.P., Ju, J., Mbow, C., Frost, P., Loveland, T., 2010. Accessing free Landsat data via the Internet: Africa's challenge. Remote Sensing Letters 1, 111–117.

Saatchi, S., Halligan, K., Despain, D.G., Crabtree, R.L., 2007. Estimation of forest fuel load from radar remote sensing. IEEE Transactions on Geoscience and Remote Sensing 45, 1726–1740.

Sader, S.A., Waide, R.B., Lawrence, W.T., Joyce, A.T., 1989. Tropical forest biomass and successional age class relationships to a vegetation index derived from Landsat TM data. Remote Sensing of Environment 28, 143–156.

Santoro, M., Beer, C., Cartus, O., Schmullius, C., Shvidenko, A., McCallum, I., Wegmüller, U., Wiesmann, A., 2011. Retrieval of growing stock volume in boreal forest using hyper-temporal series of Envisat ASAR ScanSAR backscatter measurements. Remote Sensing of Environment 115, 490–507.

Schlesinger, W.H., Andrews, J.A., 2000. Soil respiration and the global carbon cycle. Biogeochemistry 48, 7–20.

Sexton, J.O., Bax, T., Siqueira, P., Swenson, J.J., Hensley, S., 2009. A comparison of lidar, radar, and field measurements of canopy height in pine and hardwood forests of southeastern North America. Forest Ecology and Management 257, 1136–1147.

Shimada, M., Isoguchi, O., Tadono, T., Isono, K., 2009. PALSAR Radiometric and Geometric Calibration. IEEE Transactions on Geoscience and Remote Sensing 47, 3915–3932.

Simard, M., Zhang, K.Q., Rivera-Monroy, V.H., Ross, M.S., Ruiz, P.L., Castaneda-Moya, E., Twilley, R.R., Rodriguez, E., 2006. Mapping height and biomass of mangrove forests in Everglades National Park with SRTM elevation data. Photogrammetric Engineering and Remote Sensing 72, 299–311.

Siry, J.P., Cubbage, F.W., Ahmed, M.R., 2005. Sustainable forest management: global trends and opportunities. Forest Policy and Economics 7, 551–561.

Slatton, K.C., Crawford, M.M., Evans, B.L., 2001. Fusing interferometric radar and laser altimeter data to estimate surface topography and vegetation heights. IEEE Transactions on Geoscience and Remote Sensing 39, 2470–2482.

Solberg, S., Astrup, R., Gobakken, T., Næsset, E., Weydahl, D.J., 2010. Estimating spruce and pine biomass with interferometric X-band SAR. Remote Sensing of Environment 114, 2353 – 2360.

Song, C., 2012. Optical remote sensing of forest leaf area index and biomass. Progress in Physical Geography.

Stephens, B.B., Gurney, K.R., Tans, P.P., Sweeney, C., Peters, W., Bruhwiler, L., Ciais, P., Ramonet, M., Bousquet, P., Nakazawa, T., Aoki, S., Machida, T., Inoue, G., Vinnichenko, N., Lloyd, J., Jordan, A., Heimann, M., Shibistova, O., Langenfelds, R.L., Steele, L.P., Francey, R.J., Denning, A.S., 2007. Weak northern and strong tropical Land carbon uptake from vertical profiles of atmospheric CO2. Science 316, 1732–1735.

Sun, G., Ranson, K.J., 2009. Forest biomass retrieval from lidar and radar, in: Geoscience and Remote Sensing Symposium,2009 IEEE International,IGARSS 2009. Presented at the Geoscience and Remote Sensing Symposium,2009 IEEE International,IGARSS 2009, pp. V–300–V–303.

Tacconi, L., Mahanty, S., Suich, H., 2010. Payments for environmental services, forest conservation and climate change: Livelihoods in the Redd? Edward Elgar Publishing, Cheltenham, UK.

Thiel, C.J., Thiel, C., Schmullius, C.C., 2009. Operational large-area forest monitoring in Siberia using ALOS PALSAR summer intensities and winter coherence. IEEE Transactions on Geoscience and Remote Sensing 47, 3993–4000.

Torres, R., Snoeij, P., Geudtner, D., Bibby, D., Davidson, M., Attema, E., Potin, P., Rommen, B., Floury, N., Brown, M., Traver, I.N., Deghaye, P., Duesmann, B., Rosich, B., Miranda, N., Bruno, C., L'Abbate, M., Croci, R., Pietropaolo, A., Huchler, M., Rostan, F., 2012. GMES Sentinel-1 mission. Remote Sensing of Environment 120, 9–24.

Treuhaft, R.N., Law, B.E., Asner, G.P., 2004. Forest attributes from radar interferometric structure and its fusion with optical remote sensing. BioScience 54, 561–571.

Tsui, O.W., Coops, N.C., Wulder, M.A., Marshall, P.L., McCardle, A., 2012. Using multi-frequency radar and discrete-return LiDAR measurements to estimate above-ground biomass and biomass components in a coastal temperate forest. ISPRS Journal of Photogrammetry and Remote Sensing 69, 121–133.

UNFCCC, 2007. Uniting on Climate. United Nations Framework Convention on Climate Change, Bonn.

Ung, C.H., Bernier, P., Guo, X.J., 2008. Canadian national biomass equations: new parameter estimates that include British Columbia data. Canadian Journal of Forest Research 38, 1123–1132.

Van de Sand, I., 2012. Payments for ecosystem services in the context of adaptation to climate change. Ecology and Society 17, 11.

Van der Sanden, J.J., 2004. Anticipated applications potential of RADARSAT-2 data. Canadian Journal of Remote Sensing 30, 369–379.

Wackernagel, H., 2003. Multivariate geostatistics. Springer, New York.

Webster, R., 1985. Quantitative Spatial Analysis of Soil in the Field. Advances in Soil Science 3, 1–70.

Woodhouse, I.H., 2005. Introduction to Microwave Remote Sensing. Taylor & Francis.

Woods, M., Pitt, D., Penner, M., Lim, K., Nesbitt, D., Etheridge, D., Treitz, P., 2011. Operational implementation of a LiDAR inventory in Boreal Ontario. The Forestry Chronicle 87, 512–528.

Wulder, M.A., 1998. Optical remote-sensing techniques for the assessment of forest inventory and biophysical parameters. Progress in Physical Geography 22, 449 –476.

Wulder, M.A., Bater, C.W., Coops, N.C., Hilker, T., White, J.C., 2008. The role of LiDAR in sustainable forest management. The Forestry Chronicle 84, 807–826.

Wulder, M.A., Han, T., White, J.C., Sweda, T., Tsuzuki, H., 2007. Integrating profiling LIDAR with Landsat data for regional boreal forest canopy attribute estimation and change characterization. Remote Sensing of Environment 110, 123–137.

Wulder, M.A., Seemann, D., 2003. Forest inventory height update through the integration of lidar data with segmented Landsat imagery. Canadian Journal of Remote Sensing 29, 536–543.

Wulder, M.A., White, J.C., Nelson, R.F., Næsset, E., Ørka, H.O., Coops, N.C., Hilker, T., Bater, C.W., Gobakken, T., 2012a. Lidar sampling for large-area forest characterization: A review. Remote Sensing of Environment 121, 196–209.

Wulder, M.A., White, J.C., Bater, C.W., Coops, N.C., Hopkinson, C., Chen, G., 2012b. Lidar plots – a new large area data collection option: context, concepts, and case study. Canadian Journal of Remote Sensing 38, 600–618.

Xie, Y., Sha, Z., Yu, M., 2008. Remote sensing imagery in vegetation mapping: a review. Journal of Plant Ecology 1, 9–23.

Yates, F., 1948. Systematic Sampling. Philosophical Transactions of the Royal Society of London 241, 345–377.

Zhang, X., Friedl, M.A., Schaaf, C.B., 2006. Global vegetation phenology from moderate resolution imaging spectroradiometer (MODIS): evaluation of global patterns and comparison with in situ measurements. Journal of Geophysical Research 111, 1–14.

Zhu, K., Woodall, C.W., Clark, J.S., 2012. Failure to migrate: lack of tree range expansion in response to climate change. Global Change Biology 18, 1042–1052.